Supporting Materials

Structural, microstructural, and elastic-microplastic properties of wires of the aluminum-steel ACSR (AC50/8) cable after 52 years in operation, cut from different places on an overhead-power-line span

Aleksandr A. Levin[1,*], Andrei G. Panfilov[1], Alexey I. Lihachev[1], Maria V. Narykova[1], Boris K. Kardashev[1], Andrej G. Kadomtsev[1], Nikita D. Prasolov[1], Roman V. Sokolov[1], Pavel N. Brunkov[1], Makhsud M. Sultanov[2], Victor G. Kul'kov[2], Ilia A. Boldyrev[2], and Dzhonibek Sh. Norov[2]

[1] Ioffe Institute, Politekhnicheskaya ul. 26, St. Petersburg 194021, Russian Federation; a.panfilov@mail.ioffe.ru (A.G.P.), lihachev@mail.ioffe.ru (A.I.L.); maria.narykova@mail.ioffe.ru (M.V.N); b.kardashev@mail.ioffe.ru (B.K.K.); andrej.kadomtsev@mail.ioffe.ru (A.G.K.); nikpras@mail.ioffe.ru (N.D.P.); sokolovr@mail.ioffe.ru (R.V.S.); brunkov@mail.ioffe.ru (P.N.B.)

[2] "Moscow Power Engineering Institute", National Research University, Volzhsky branch, Lenina pr. 69, Volzhsky 404110, Russian Federation; sultanov_mm@mail.ru (M.M.S.); vikulkov@yandex.ru (V.G.K.); boldyrev@vfmei.ru (I.A.B.); jonibeck.norov@mail.ru (D.S.N.)

[*] Correspondence: aleksandr.a.levin@mail.ioffe.ru (A.A.L.)

S1. Samples

S.1. Samples

Samples of aluminum and steel wires cut from Aluminum Conductor Steel Reinforced (ACSR) cables of AC50/8 modification (with areas of aluminum and steel parts of ≈50 mm^2 and ≈8 mm^2, respectively) had a cylindrical shape. Their length l, base diameter Ø measured with a certified caliper, as well as the integral density ρ according to the results of densitometric measurements are shown in Table S1.

Table S1. Sizes (diameter Ø and length l) of cylindrical aluminum and steel wire samples, which were cut from the cable from different places on an overhead-power-line span for the XRD and acoustic studies, and their mass density ρ according to densitometric measurements. Service life of the N1, N2, and N3 wires is equal to 52 years. Samples N0 are new (0 years of service life).

Sample	Wire material	Span part	l, мм	Ø, мм	ρ, g/cm^3
N0_W	Al	–1[a]	25.11	3.18	2.6967(3)
N1_W	Al	0/1	25.10	3.23	2.6846(3)
N2_W	Al	1/4	25.11	3.25	2.6830(3)
N3_W	Al	1/2	25.17	3.24	2.6872(3)
N0_C	steel	–1[a]	27.06	3.20	7.7462(8)
N1_C	steel	0/1	26.78	3.25	7.5650(8)
N2_C	steel	1/4	27.00	3.22	7.6150(8)
N3_C	steel	1/2	27.12	3.23	7.6828(8)

[a] designation of span part for new cable (service life of 0 years)

The choice of the length l of the samples was made based on the formula [1] for the individual frequency of the sample in the acoustic method of the composite resonant vibrator

$$f = f_{\mathrm{qs}} + \frac{m_q}{m}\left(f_{\mathrm{qs}} - f_{\mathrm{q}}\right), \quad \text{(S1)}$$

where m is the mass of the sample, m_{q} is the mass of the piezoelectric quartz, f_{qs} is the frequency of the piezoquartz-sample composite system, and f_{q} is the frequency of the piezoelectric quartz. The length of the samples was selected in such a way that in acoustic measurements the chosen length provided the individual frequency of the composite vibrator (piezoelectric quartz + rod-like (cylindrical) sample) close to the frequencies of the piezoelectric quartz and the sample, and so that the resonant frequency of longitudinal vibrations of the sample was about 100 kHz.

For ease of use, the nomenclature of wires cut from the new (service life of 0 years) cable and from the cable operated during 52 years in an overhead power line (OPL) is summarized in Table S2.

Table S2. Wire samples investigated.

Sample	Service life, years	Location	Designation of location	Nominal wire material	Contact
N0_C	0	~1 m from the end of the new coil of cable	-1[a]	steel (electroplated with Zn)	steel wire core – Al wire
N0_W	0	~1 m from the end of the new coil of cable	-1[a]	aluminum	any (Al wire – air or Al wire – steel wire core)
N1_C or N1_C-W	52	next to the clamp of the tension cable-garlands (near to the OPL support)	0/1	steel (electroplated with Zn)	steel wire core – Al wire
N1_W-A	52	next to the clamp of the tension cable-garlands (near to an OPL support)	0/1	aluminum	Al wire – air
N1_W-C	52	next to the clamp of the tension cable-garlands (near to an OPL support)	0/1	aluminum	Al wire – steel wire core
N2_C or N2_C-W	52	quarter the span length between the adjacent supports of OPL	1/4	steel (electroplated with Zn)	steel wire core – Al wire
N2_W-A	52	quarter the span length between the adjacent supports of OPL	1/4	aluminum	Al wire – air
N2_W-C	52	quarter the span length between the adjacent supports of OPL	1/4	aluminum	Al wire – steel wire core
N3_C or N3_C-W	52	half the span length between the adjacent supports of OPL	1/2	steel (electroplated with Zn)	steel wire core – Al wire
N3_W-A	52	half the span length between the adjacent	1/2	aluminum	Al wire – air

		supports of OPL			
N3_W-C	52	half the span length between the adjacent supports of OPL	1/2	aluminum	Al wire – steel wire core

[a] designation of span part for new cable (service life of 0 years)

S.1.2. Estimates of penetration depth of X-rays for maximum diffraction angle

Let us dwell on such important points as the size of the regions and the thickness of the near-surface layers of wires, which have been the objects of study by various methods listed above.

The OM images and XRD patterns were obtained from the outer (long) side of the cylinder-like wire specimens. The EDX spectra were taken both from the outer side of the wires and from the facets of their cross-sections. The EBSD maps were constructed from facets of wire cross-sections. The SEM pictures were only used to control the surface quality of the cross-sections for EBSD maps.

The EDX analysis was carried out from areas of 500 x 500 μm² in the center of the samples (either cross-sections or the long sides of cylinder-like wire samples). The EBSD maps were constructed with a step of 0.5 μm from areas of 500 x 500 μm² in the center of the wire cross-sections and at a distance of ~150 μm from the edge of the surface of the wires in contact with neighboring wires (i.e., with an adjacent Al wire for a steel core wire, and, conversely, with a steel core wire for an Al wire) and, in the case of an Al wire, with the atmosphere. According to [2, 3], in NSL ~150 μm thick, 99.99% of the total change in density from its value in the bulk occurs from the surface of the wires due to the formation of defects of a void nature after the operation of wires in overhead OPL cables.

In the EDX and EBSD measurements (as in SEM studies), electrons with energy E_0 fall on the surface of the sample and penetrate inside to the diffusion depth. A review of approaches to estimating the electron penetration depth from which a signal is recorded is given in [4]. According to the Kanaya-Okayama model [5] most commonly used in the literature, the maximum penetration depth R_{K-O} of electrons into the solid matter is estimated as

$$R_{K-O}(\mu m) = \frac{0.0276 \cdot A \cdot E_0^{5/3}}{\rho \cdot Z^{8/9}}, \quad \text{(S1)}$$

where A (g/mol), Z, and ρ (g/cm³) are, respectively, the molar mass, atomic number, and integral density of the sample material (values averaged over the sample if it consists of several crystalline phases). If one takes as ρ of aluminum and steel wires their nominal densities, which are 2.70 g/cm³ and 7.80 g/cm³ according to the manufacturer's certificate GOST 839 [6], respectively, then the maximum values of R_{K-O} at an electron beam energy of E_0 = 15 keV will be ≈2–3 μm and ≈1 μm in the case of aluminum and steel wires, respectively, for elements from O (Z = 8) to Zn (Z = 30), the presence of some of which is observed according to the EDX spectra. Other models reviewed in [4] give close values of the penetration depth of electrons into the solid matter.

The XRD measurements were carried out either with a sample rotation around an axis coinciding with the diffractometer axis (in order to average out the effects of preferential orientation of crystallites in the wire) or without rotation, when the long side of the sample was fixed parallel to the rectangular focus of the X-ray tube beam illuminating an area of ~8x0.04 mm² on the sample surface. An illustration of the

geometry of the XRD survey and a discussion of the difference in the obtained XRD patterns are given in [2]. The XRD patterns obtained with rotation during recording were used to analyze the effects of preferential orientation in wires. The computations of the structural and microstructural characteristics of the wires were carried out using XRD patterns measured from a fixed long side of the wires.

The samples from which XRD patterns were recorded were solid pieces of wires. Therefore, the main contribution to the XRD pattern during measurements was made only by the NSL of the wires. For the X-ray radiation, the characteristic that gives an idea of the thickness of this NSL is the X-ray penetration depth, T_{pen}, which is understood as the thickness of the layer from the surface, from which the reflected X-ray beam arrives attenuated by a factor of $e \approx 2.72$ compared to the intensity of the beam incident on the surface. In the case of a symmetric 2θ-θ scan mode for maximum angle of diffraction 2θ from a material with known mass attenuation (absorption) μ_l and mass density ρ

$$T_{\text{pen}} = \frac{\sin(\theta)}{2 \cdot \mu_l \cdot \rho} \tag{S2}$$

(see [2] for a descriptive graphical illustration). For crystalline phases other than Al, calculated X-ray densities ρ_X given in Powder Diffraction File (PDF-2) database [7] cards were used for estimation of T_{pen}. For Al, the theoretical mass density $\rho_{\text{calc}} = \rho_X$ is then taken as the mass density ρ calculated from the structural data as the ratio of the mass $M_{\text{cell}} = Z \cdot A_r$ of an elementary cell to its volume V_{cell} (A_r is the molecular weight of the formula unit of the material, Z is the number of formula units in the elementary cell). Accordingly, for ρ_X in g/cm^3, V_{cell} in Å^3 and A_r in in Da (i.e., atomic mass unit (a.m.u.) or g/mol) the standard expression leads to the formula

$$\rho_X = \frac{Z \cdot A_r}{N_A \, V_{cell} \cdot 10^{-24}}, \tag{S3}$$

where N_A = 6.02214076·10^{23} mol^{-1} is the Avogadro number [8]. For Al phase with parameter a of cubic unit cell,

$$V_{\text{cell}} = a^3. \tag{S4}$$

To estimate T_{pen}, the values of the linear absorption coefficient μ_l were used calculated by the program *PowderCell* 2.4 [9] in accordance with the structural models of the observed crystallographic phases from the Crystallographic Open Database (COD) [10]. In estimating the T_{pen} of the δ- and δ*-Al_2O_3 phases [11, 12], for which there are no completed structural models, the linear absorption coefficient μ_l of the δ-Al_2O_3 modification from [13] was used.

Taking as the maximum angle the diffraction angle $2\theta = 141°$, which is the maximum for XRD measurements in this study, then, for Al, which is the main material in Al wires, estimates (see Table S3 of Supporting Materials) give $T_{\text{pen}} \approx 36$ μm, $T_{\text{pen}} \approx 11$ μm for the Zn material of the galvanic layer of steel wires, and $T_{\text{pen}} \approx 1.9$ μm in the case of Fe as the main material of steel wires after the destruction of the galvanic layer. In the case of oxide formation, the T_{pen} values increase to ≈37 μm for δ - and δ*-Al_2O_3, ≈13.4 μm for ZnO, ≈19 μm for ZnO_2, ≈3.2 μm for α-FeO, and ≈4.5 μm for γ-Fe_2O_3. However, it should be taken into account that it is unlikely that oxides form continuous layers, but rather only inclusions in the base material (aluminum for Al wires and Zn and/or Fe for steel wires, depending on the degree of destruction of the galvanic protective layer). Therefore, it is possible that the reflections also come from a slightly greater depth from the surface of the samples.

Estimates of the penetration depths T_{pen} for different possible crystalline phases according to formula (S2) are presented in Table S3. Half the maximum diffraction angle $2\theta = 141°$ of the XRD measurements (Cu-K_α radiation) was utilized for calculation of the T_{pen} estimates.

Table S3. Estimates of the penetration depths T_{pen} for different possible crystalline phases for maximum diffraction angle $2\theta = 141°$ (Cu-K_α radiation).

Crystalline phase	Space group	T_{pen}, μm	PDF-2 card	Ref.
Al	$Fm\bar{3}m$ (225)	35.9	01-073-9843	[14]
δ-Al_2O_3	$P4_12_12$ (92)	37.5 [a]	00-056-1186	[11]
δ*-Al_2O_3	$P222$ (16)	37.4 [a]	00-066-1215	[12]
Zn	$P6_3/mmc$ (194)	10.9	01-080-4436	[15]
ZnO	$Fm\bar{3}m$ (225)	13.4	01-073-8589	[16]
ZnO_2	$Pa\bar{3}$ (205)	19.0	01-076-1364	[17]
Fe	$Im\bar{3}m$ (229)	1.9	00-006-0696	[18]
α-FeO	$Fm\bar{3}m$ (225)	3.2	01-080-3819	[19]
γ-Fe_2O_3	$P4_32_12$ (96)	4.5	01-089-5894	[20]

[a] The linear absorption coefficient μ_l calculated for a modification of δ-Al_2O_3 (tetragonal space group $P\bar{4}m2$ (115)) [13] was used for estimation of T_{pen}.

S2. Results

Similar to main text, to explicitly show the periodicity of changes in the characteristics of the material of the wires along the span length between the OPL supports when presenting the quantitative results of EBSD, XRD, densitometric and acoustic measurements on graphs of the Supporting Materials, the points for the span parts '3/4' and '1/1' are set by mirroring the experimental points at the span parts '1/4' and '0/1', respectively. Lines of different styles connecting the experimental points on the graphs, which were shown with different symbols for different samples according to the legends depicted in the Figures, are guides to the eye only. The data for samples from the new cable are indicated at the position on the span formally equal to '–1'.

S2.1. Results of OM

Figures S1a,b,c,d show OM images of the surfaces of samples of aluminum and steel wires N1 (0/1 span) and N3 (1/2 span) cut from an AC50 type ACSR cable that served 52 years in an OPL in the Volgograd region of Russia. For comparison, OM images of the surfaces of samples

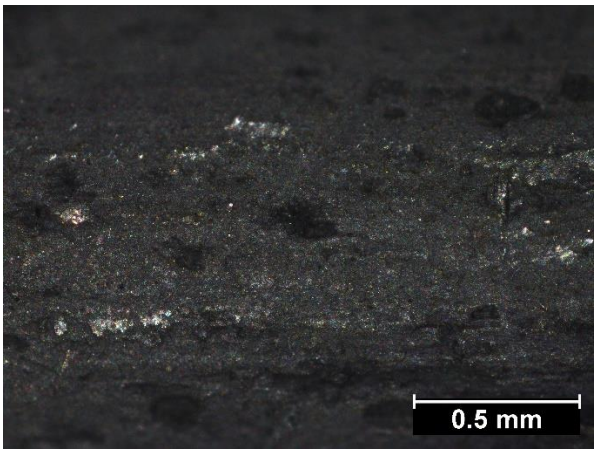

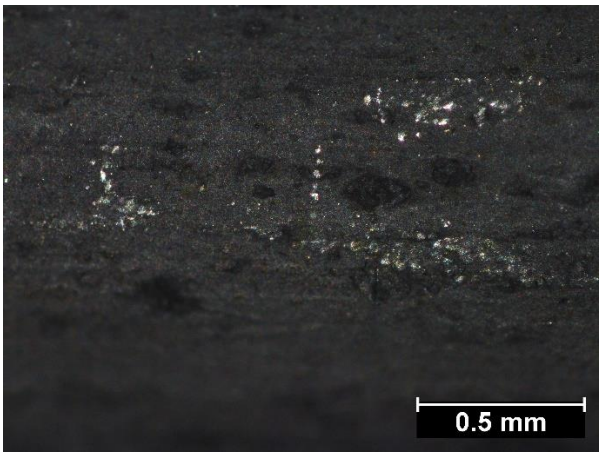

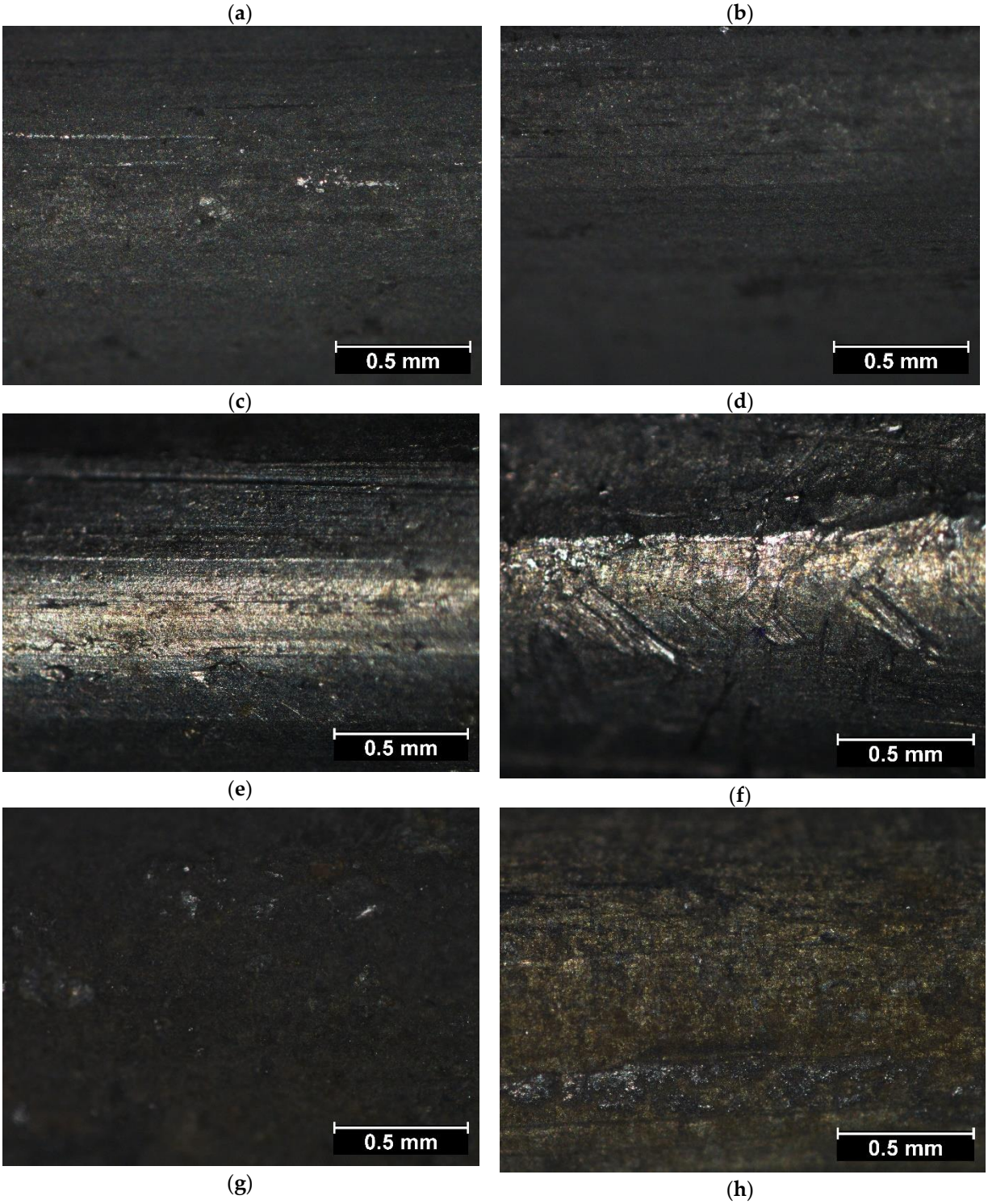

Figure S1. OM images of Al wires (**a**) N1_W-A, (**b**) N1_W-C, (**c**) N3_W-A, (**d**) N3_W-C, (**e**) N2-2_W-A, (**f**) N2-2_W-C, and steel wires (g) N1_C-W and (h) N3_C-W. Wires N1 (0/1 span) and N3 (1/2 span) are cut from the AC50 cable after 52 years of exploitation in air OPL. Wire N2-2 (the same as investigated in Ref. [3]) is cut from the AC50 cable after 8 years of exploitation in air OPL. W-C and W-A are contacts of an Al wire with a steel core, and an Al wire with air atmosphere, respectively.

of N2-2 Al wires (previously studied in [3]) cut from a cable of the same type and brand and served in the same area for 8 years are also shown. Surfaces are shown near the contacts of Al wires with the atmosphere (the W-A contacts, Figures S1a,c,e) and with steel wire (the W-C

contacts, Figures S1b,d,f). For steel wires, C-W contact surfaces with adjacent Al wires are shown.

S2.2. Results of EDX

Figures S2a,b show the EDX spectra from the surface of the long (outer) side of new unused samples of steel (N0_C) and aluminum (N0_W) wire cut from a coil of a new cable. More precisely, Figure S2b shows the EDX spectrum recorded from that side of aluminum wire which was in contact with the atmosphere (i.e., the spectrum for N0_W-A). However, since the wire is new, the EDX spectrum taken from the surface that was in contact with the steel core wire (N0_W-C) is similar to that shown in Figure S2b. Figures S2c,d,e,f,g,h,i,k,l give the EDX spectra from the surface of the long (outer) side of steel (Figures S2c,f,i) and aluminum (Figures S2d,e,g,h,k,l) cable wires after 52 years of service at the beginning of the span (0/1 span, Figures S2c,d,e), at a quarter span (1/4 span, Figures S2f,g,h) and half span (1/2 span, Figures S2 i,k,l) of the OPL length between supports. For all steel core wires, the EDX spectra were recorded from the C-W surfaces of these wires, which were in contact with aluminum wires, since the core consists of only one steel wire in the ACSR cables of the A50 brand. For aluminum wires, the EDX spectra were recorded both from the W-A surfaces in contact with the atmosphere (Figures S2d,g,k) and from the W-C surfaces in contact with the steel core wire (Figures S2e,h,l). Since the EDX spectra obtained from the wire cross-sections for all samples, including new and after 52 years of operation, are almost identical, Figures S2m,n show as an example the EDX spectra detected from the cross-sections of the steel (N2_C) and aluminum (N2_W) wires of the sample N2, cut from the cable at a quarter of the span between the supports (1/4 span).

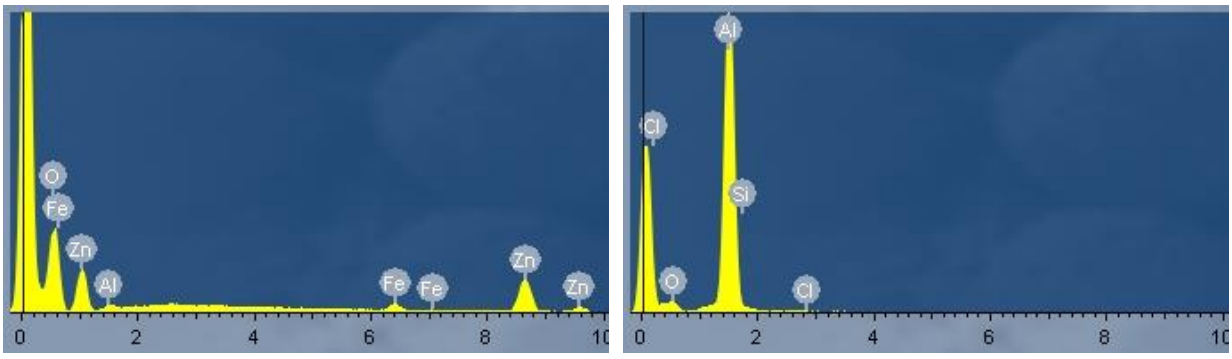

(**a**)

(**b**)

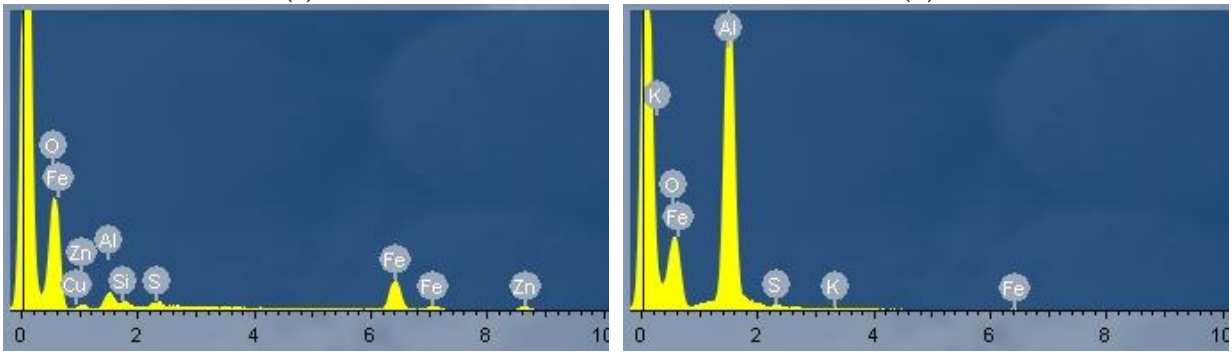

(**c**)

(**d**)

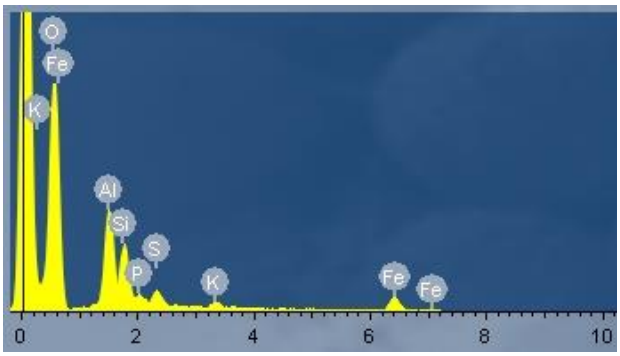
O
Fe
K
Al
Si
S
P
K
Fe
Fe
0
2
4
6
8
10

(**e**)

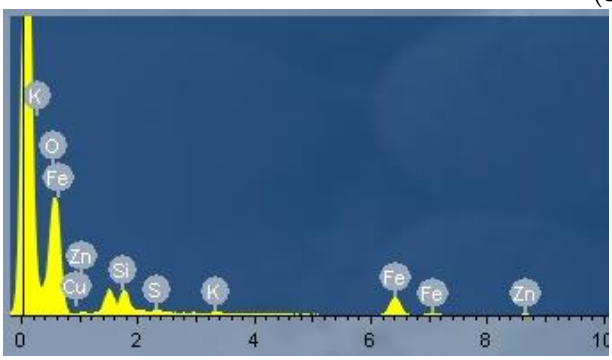
K
O
Fe
Zn
Cu
Si
S
K
Fe
Fe
Zn
0
2
4
6
8
10

(**f**)

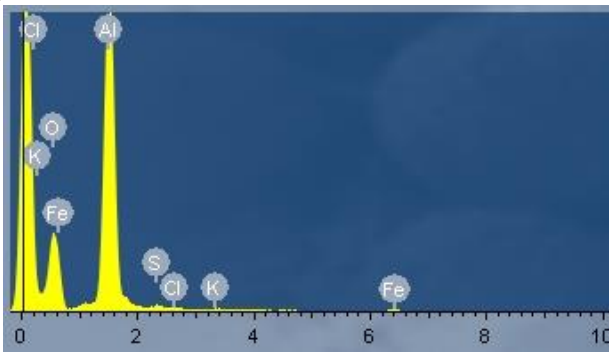
Cl
Al
O
K
Fe
S
Cl
K
Fe
0
2
4
6
8
10

(**g**)

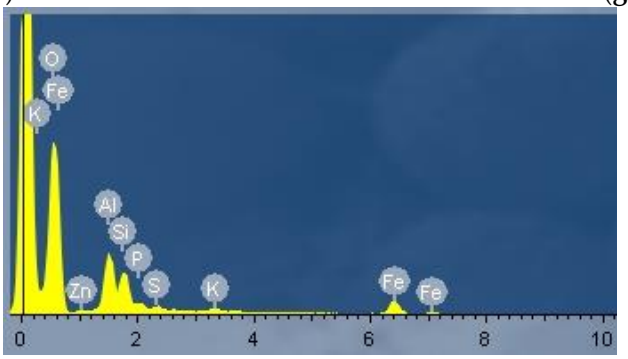
O
Fe
K
Al
Si
P
Zn
S
K
Fe
Fe
0
2
4
6
8
10

(**h**)

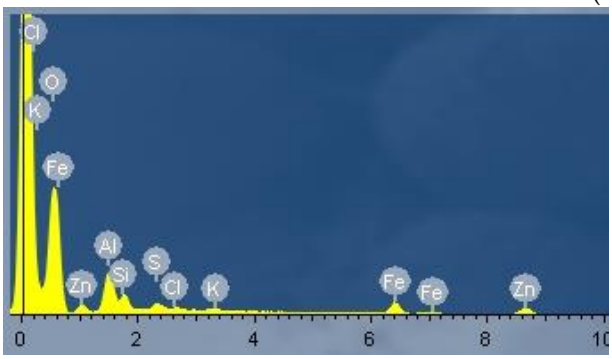
Cl
O
K
Fe
Al
S
Zn
Si
Cl
K
Fe
Fe
Zn
0
2
4
6
8
10

(**i**)

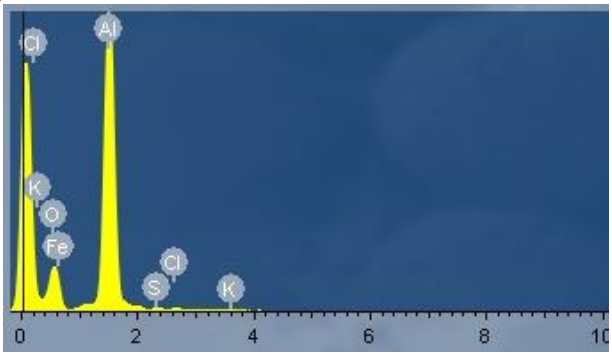
Cl
Al
K
O
Fe
Cl
S
K
0
2
4
6
8
10

(**k**)

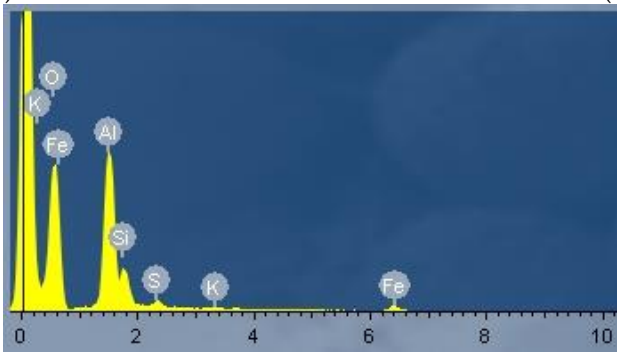
O
K
Fe
Al
Si
S
K
Fe
0
2
4
6
8
10

(**l**)

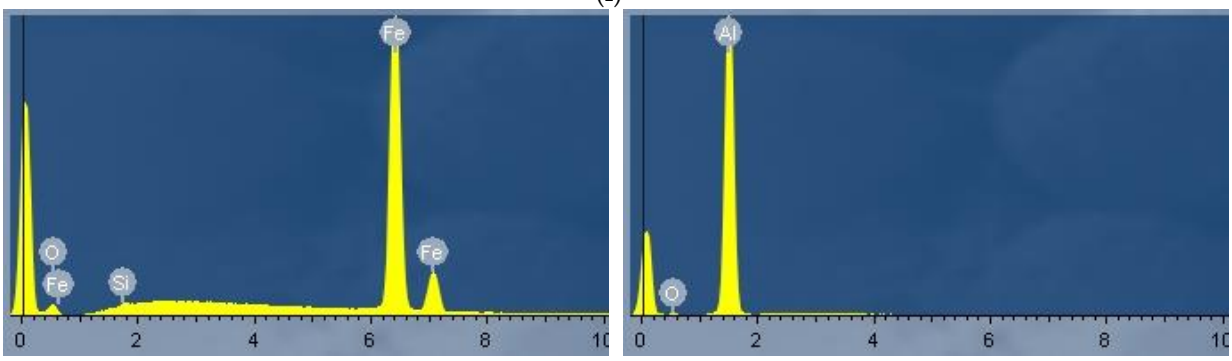

(**m**) (**n**)

Figure S2. EDX spectra obtained from the long (external) side of the samples (**a**) N0_C, (**b**) N0_W, (**c**) N1_C-W, (**d**) N1_W-A, (**e**) N1_W-C, (**f**) N2_C-W, (**g**) N2_W-A, (**h**) N2_W-C, (**i**), N3_C-W, (**k**) N3_W-A, and (**l**) N3_W-C and EDX spectra registered from the centers of the cross-sections of the wires (**m**) N2_C and (**n**) N2_W. Samples N0 are new samples cut from an AC50 cable coil. Samples N1, N2, and N3 of wires are cut off from an AC50 cable in places, respectively, near the supports (0/1 span) and at a distance of a quarter (1/4 span) and half (1/2 span) of the span length between the supports after 52 years of operation in OPL. 'A', 'W' and 'C' correspond to the air (atmosphere), aluminum wire, and steel wire core, respectively. Correspondingly, 'W-A' and 'W-C' are the aluminum wire surfaces near contacts between aluminum wire and either atmosphere or steel wire core. 'C-W' is a surface of the steel wire in contact with the aluminum wires.

S2.3. Results of EBSD

Figure S3 gives EBSD maps of aluminum (Figures S3a,b,c,d,e,f) and steel wires (Figures S3g,h,i,l) cut from a cable that has served 52 years in an OPL. Samples N1_W and N1_C (respectively, aluminum and steel wire, Figures S3a,b,c and S3g,h,i) were cut from the cable location near the clamps of the OPL supports (0/1 span). Samples N31_W and N1_C

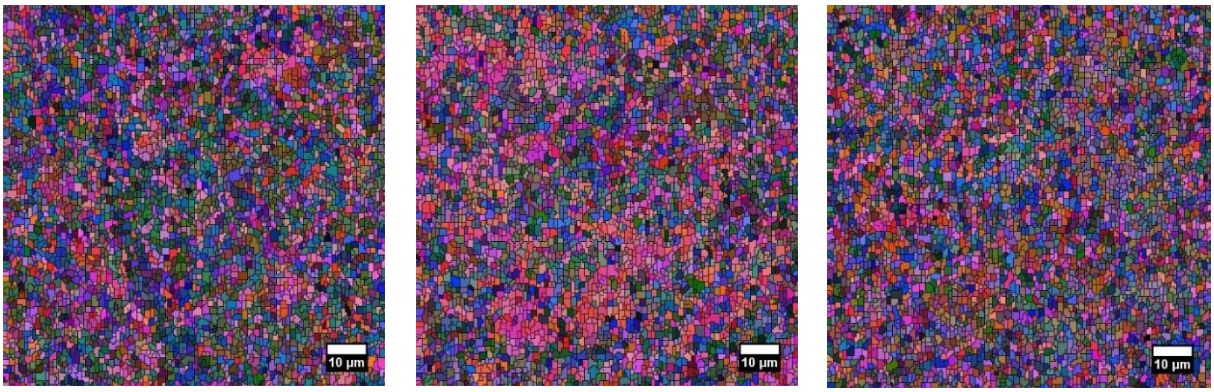

(**a**) (**b**) (**c**)

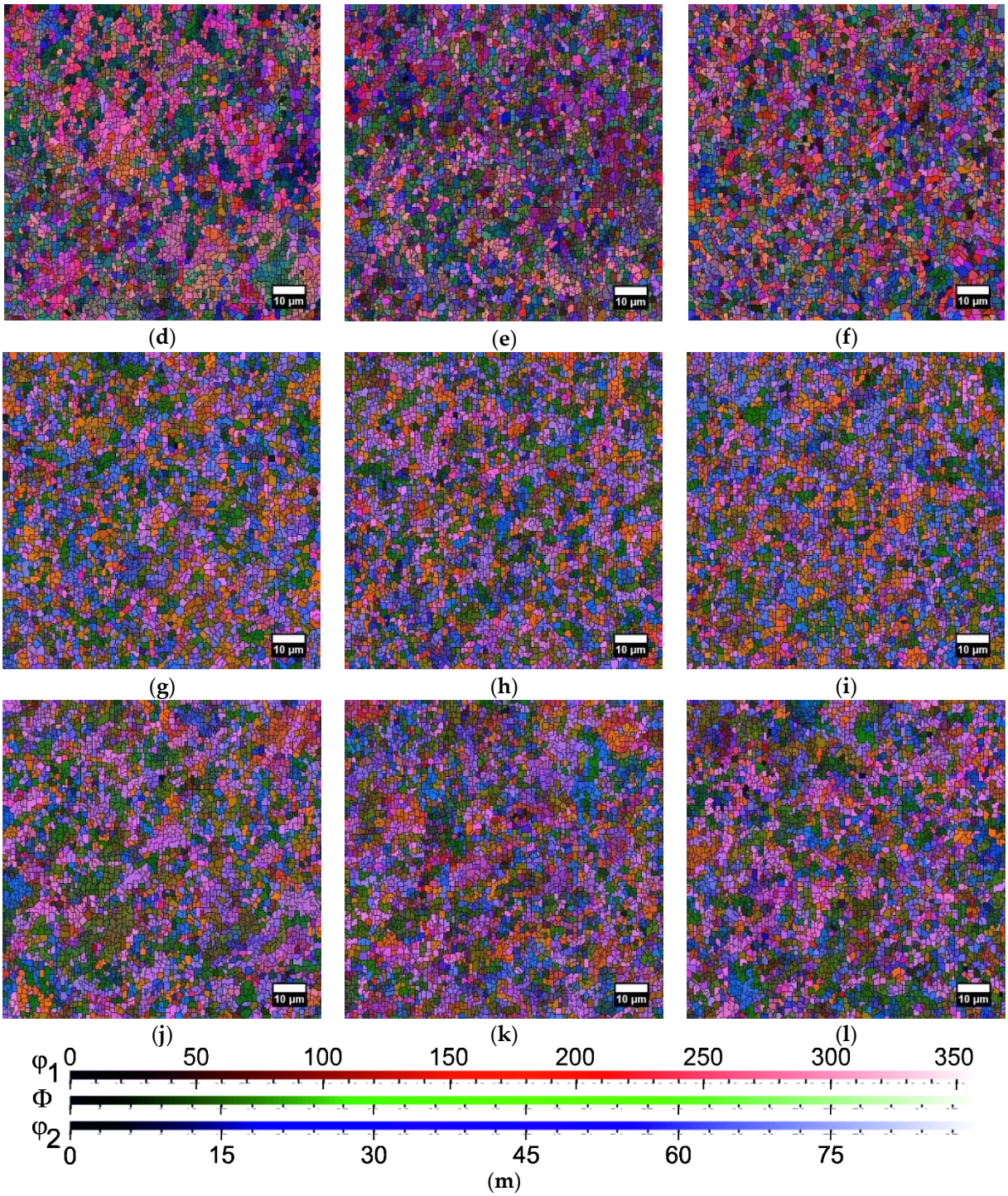

Figure S3. EBSD distribution maps of the Euler angles φ_1, Φ, and φ_2 of the cross-sections of aluminum (**a**, **b**, **c**) N1_W (0/1 span) and (**d**, **e**, **f**) N3_W (1/2 span) wires, and steel core (**g**, **h**, **i**) N1_C (0/1 span) and (**j**, **k**, **l**) N3_C (1/2 span) wires from the AC50 cable after 52 years of operation in an OPL. EBSD maps shown in (**a**, **d**, **g**, **j**) were taken from the area in the center of the aluminum (**a**, **d**) and steel-core wire cross-section (**g**, **j**). For aluminum wires, the EBSD maps were registered from the area W-C of the contact with the adjacent steel-core wire (**b**, **e**) and from the contact W-A of the aluminum wire with the surrounding air (**c**, **f**). For steel-core wires, the EBSD maps were obtained from the area C-W of the contact with the adjacent aluminum wire (**h**, **k**) and from the second contact C-W(2) with the adjacent aluminum wire at opposite side of the steel-wire cross-section (**i**, **l**). Legends and scales (in degrees) of the Euler angles are shown in (**m**). The angle range of Φ is the same as that of φ_2.

(respectively, aluminum and steel wires, Figures S3d,e,f and S3j,k,l) were cut from the cable from a location in the middle of the span between the OPL supports (1/2 span).

Figure S4 shows grain-size distribution histograms for aluminum (Figures S4a,b) and steel (Figures S4c,d) wires from cable after 52 years of service in OPL, which were cut from the span between OPL supports at locations near the support's clamp (aluminum N1_W and steel N1_C wires, 0/1 span, Figures S4a,c) and at half span (1/2 span) between supports (aluminum N3_W and steel N3_C wires, Figures S4b,d).

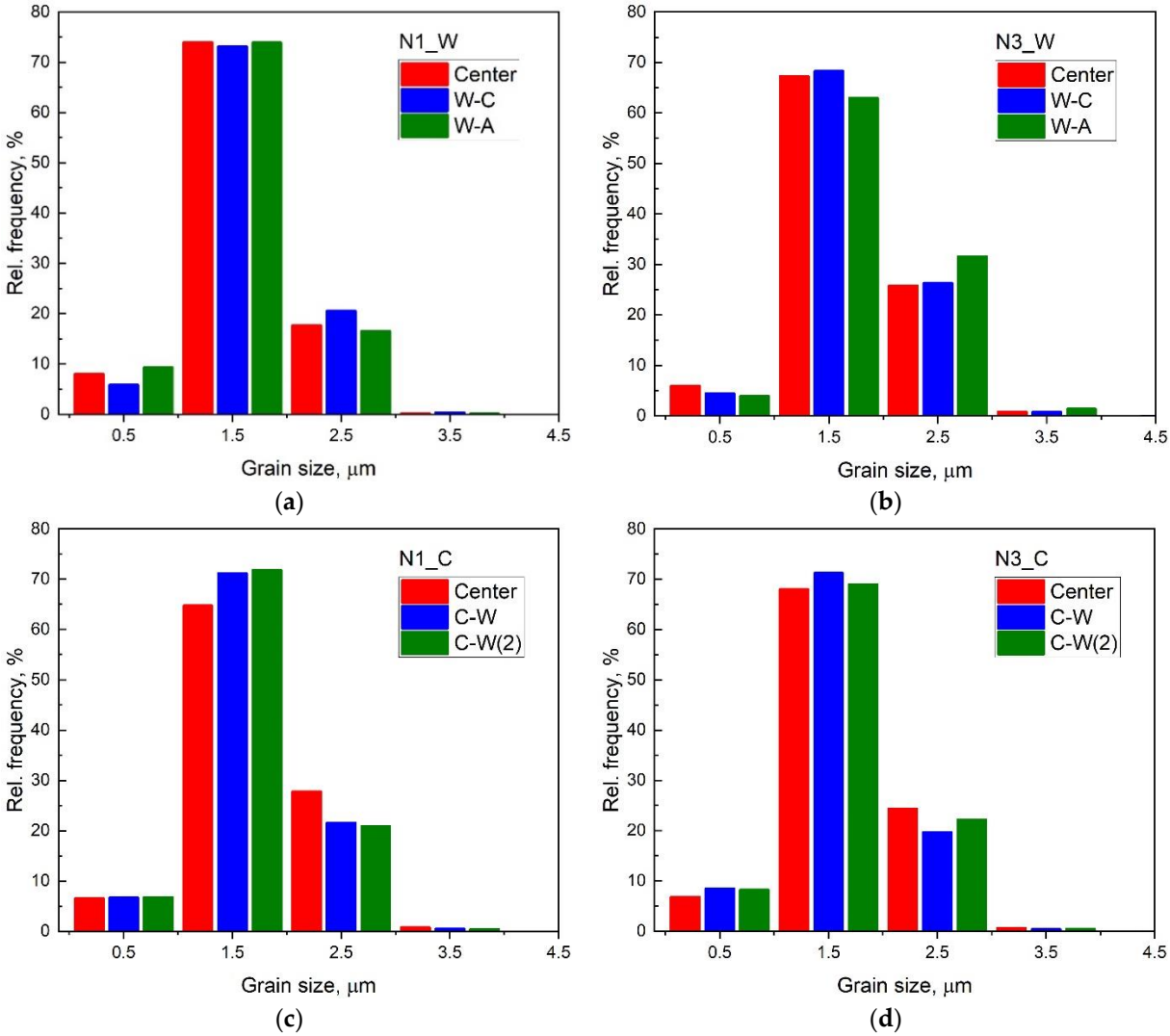

Figure S4. Grain-size distribution histograms in the central and edge areas of the cross-sections of aluminum wires (**a**) N1_W (0/1 span) and (**b**) N3_W (1/2 span) and steel wire cores (**c**) N1_C (0/1 span) (**d**) N3_C (1/2 span) from the AC50 cable after 52 years of operation in an OPL. Histograms designated as 'Center' were obtained from the centers of the wire cross-sections. Histograms designated as W-C and W-A were obtained from areas of aluminum wires near contacts of aluminum wire – steel wire core and aluminum wire – surrounding air, respectively. Histograms designated as C-W and C-W(2) were calculated from areas of steel wire cores near contacts of steel wire – adjacent aluminum wire and steel wire – adjacent aluminum wire at opposite side of the steel wire. For better visualization, the Center and W-A (or W-C(2)) histogram columns are shifted along the abscissa axis by the width of the base of the histogram columns, respectively, to the left and to the right relative to the true position.

Figure S5 shows relative areas S_{rel} occupied by grains in dependence on the grain sizes D_{grain} for samples N2 (1/4 span) and N3 (1/2 span) after 52 years of operation in an OPL.

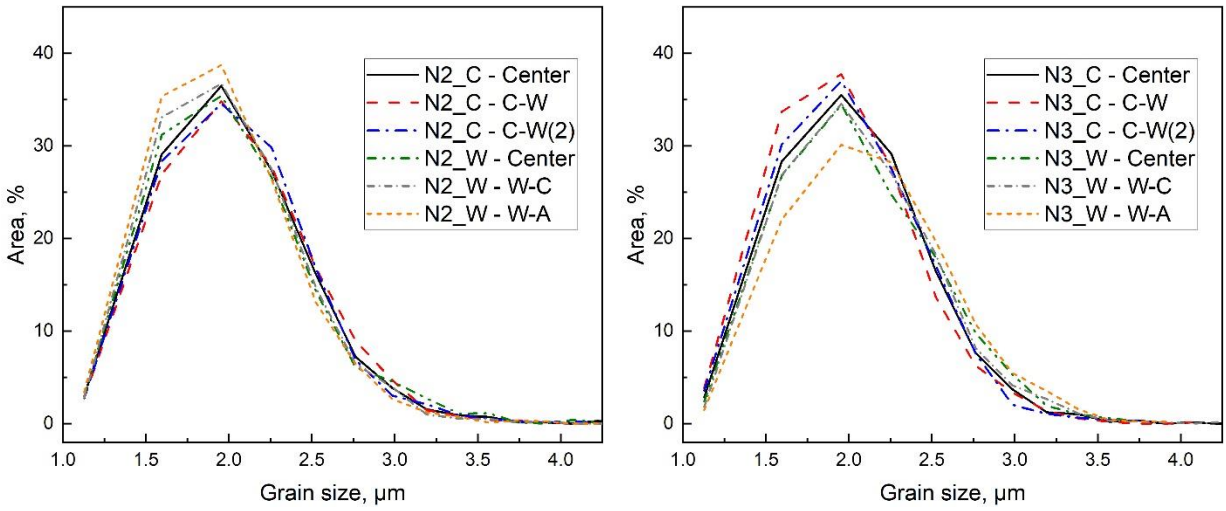

(**a**) (**b**)

Figure S5. Relative areas S_{rel} occupied by grains in dependence on the grain sizes D_{grain} in (**a**) N2 (1/4 span) and (**b**) N3 (1/2 span) after 52 years of operation in an OPL. The aluminum sample are designed as '_W', whereas the steel wires are shown with '_C' designation. Explanations of the 'Center', W-C, W-A, C-W, and C-W(2) designations are given in caption to Figure S4.

It should be noted that, when either the distribution of grains by size (Figure 3 of main text and Figure S4) or the dependence of S_{rel} on the grain size (Figure S5) is discussed, the size of each particular grain D_{grain} refers to the effective diameter of a round grain with the same area as the actually observed grain has (calculated using the applied EBSD map analysis program).

Figure S6 gives grain distribution histograms by their aspect ratios (ARs) for aluminum (Figures S6a,b) and steel (Figures S6c,d) wires from a 52 year OPL cable cut at locations near the support's clamp (aluminum N1_W and steel N1_C wires, 0/1 span, Figures S6a,c) and half a span between OPL supports (aluminum N3_W and steel N3_C wires, 1/2 span, Figures S6b,d).

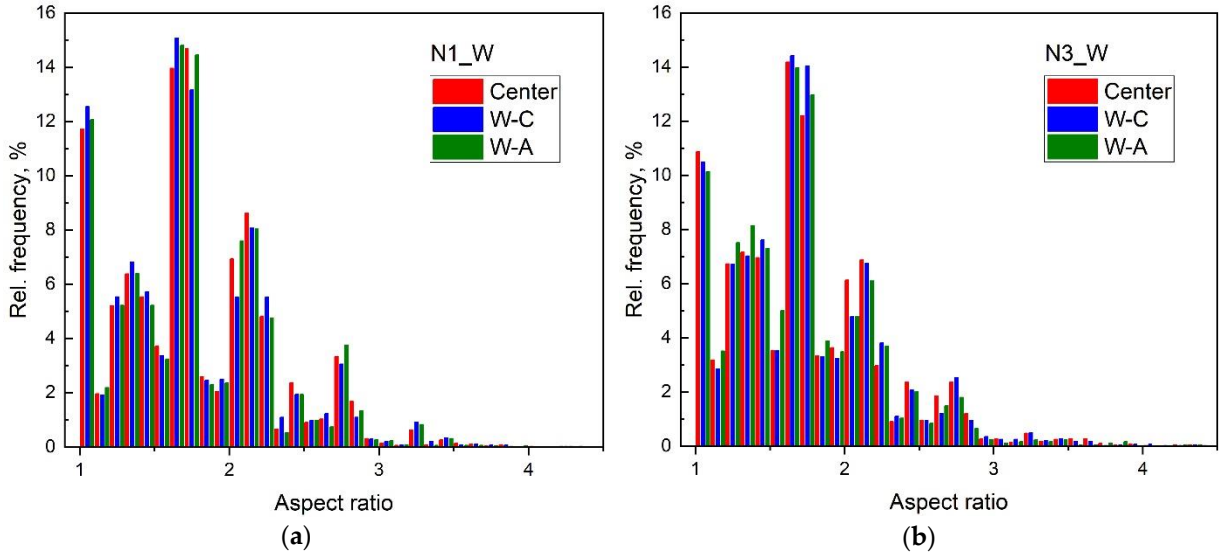

(**a**) (**b**)

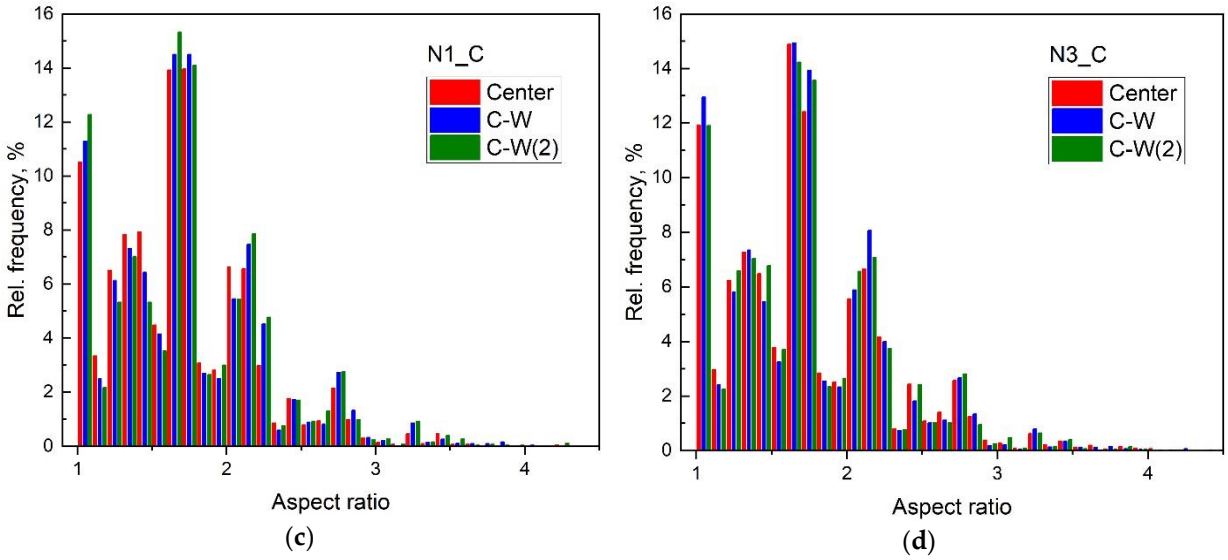

Figure S6. AR distribution histograms in the central and edge areas of the cross-sections of aluminum wires (**a**) N1_W (0/1 span) and (**b**) N3_W (1/2 span) and those of steel wire cores (**c**) N1_C (0/1 span) (**d**) N3_C (1/2 span) from the AC50 cable after 52 years of operation in an OPL. Explanations of W-C, W-A, C-W, and C-W(2) designations are given in caption to Figure S4. For better visualization, the Center and W-A (or W-C(2)) histogram columns are shifted along the abscissa axis by the width of the base of the histogram columns, respectively, to the left and to the right relative to the true position.

Quantitative characteristics of the microstructure of samples obtained from the analysis of grain size distributions (Figures S4a,b,c,d and Figures 3a,b,c,d of main text), ARs (Figures S6a,b,c,d and Figures 5a,b,c,d of main text) and misorientation angles of grain boundaries (GBs, Figures 6a,b,c,d,e,f,g,h of main text) are presented in Table S4. In this Table S4, for all investigated cross-sections of samples of aluminum wires (W) and steel core wires (C) in their middle and at the point of contact with other wires (W-C, C-W, and C-W(2)) or air atmosphere (W-A), we give average grain sizes $\langle D_{grain} \rangle$, relative areas S_{rel}^{max} (relative areas occupied by grains and measured at the maximum of the dependence $S_{rel}(D_{grain})$ observed at grain size D_{grain} = 1.95 μm), fractions $f_{AR<3.2}$ of grains with aspect ratios AR < 3.2, average values $\langle AR \rangle$ of aspect ratios of grains, fractions $f_{=2}$ and f_{HAGB} of GBs with misorientation angles φ_{mis} = 2°, 2° < φ_{mis} < 15° (low-angle GBs (LAGBs)) and φ_{mis} ≥ 15° (high-angle GBs (HAGBs)), respectively, average misorientation angles $\langle \varphi_{mis}^{LAGB} \rangle$, $\langle \varphi_{mis}^{HAGB} \rangle$, and $\langle \varphi_{mis} \rangle$ for LAGBs, HAGBs, and the GBs altogether (φ_{mis} ≥ 2°), respectively.

Table S4. Microstructure characteristics of the aluminum wires (W) and steel wire core (C) at different locations of the cross-section of the wires from the AC50 cable after 52 years of operation in OPL, obtained by analysis of the distribution histograms of the grain sizes (mean grain sizes $\langle D_{grain} \rangle$, relative areas S_{rel}^{max} occupied by grains with size D_{grain} = 1.95 μm (where maximum of the $S_{rel}(D_{grain})$ dependence is observed), grain ARs (fraction $f_{AR<3.2}$ of grains with AR < 3.2), and mean values $\langle AR \rangle$ averaged over all AR values observed) and misorientation angles of the GBs (fractions $f_{=2}$,[a] f_{LAGB} [a] and f_{HAGB} [a] of GBs with misorientation angle φ_{mis} = 2°, LAGBs (2° < φ_{mis} < 15°), and HAGBs (φ_{mis} ≥ 15°), respectively; mean misorientation angles $\langle \varphi_{mis}^{LAGB} \rangle$ and $\langle \varphi_{mis}^{HAGB} \rangle$ of the LAGBs and HAGBs, respectively; and mean misorientation angles $\langle \varphi_{mis} \rangle$ averaged over whole φ_{mis} range (φ_{mis} ≥ 2°).

Sample	**Location**	$\langle D_{grain} \rangle$,	S_{rel}^{max},	$f_{AR<3.2}$,	$\langle AR \rangle$	$f_{=2}$,	f_{LAGB},	f_{HAGB},	$\langle \varphi_{mis}^{LAGB} \rangle$,	$\langle \varphi_{mis}^{HAGB} \rangle$,	$\langle \varphi_{mis} \rangle$,

(Span)		μm	%	%		%	%	%	degr.	degr.	degr.
N0_W	Center	1.66	34.44	98.39	1.73	23.0	34.75	42.25	8.08	29.75	15.84
(-1) [b]	W-C	1.62	40.38	99.09	1.69	18.9	11.74	69.36	8.79	37.86	27.67
	W-A	1.63	39.18	98.90	1.72	17.6	12.75	69.65	8.85	38.16	28.06
N1_W	Center	1.60	40.98	99.25	1.72	13.9	11.40	74.70	8.82	38.93	30.36
(0/1)	W-C	1.64	38.67	99.09	1.71	16.3	13.14	70.56	8.94	38.46	28.63
	W-A	1.58	43.47	99.32	1.72	14.4	11.37	74.23	8.90	38.34	29.76
N2_W	Center	1.67	35.40	98.53	1.74	22.6	25.68	51.72	8.56	36.08	21.31
(1/4)	W-C	1.65	36.72	98.64	1.72	19.4	19.29	61.31	8.47	38.06	25.36
	W-A	1.62	38.73	98.93	1.73	20.9	22.80	56.30	8.48	35.65	22.42
N3_W	Center	1.72	34.44	98.57	1.70	21.0	26.57	52.43	8.38	36.80	22.06
(1/2)	W-C	1.73	34.13	98.78	1.69	21.4	20.12	58.48	8.37	38.72	24.86
	W-A	1.79	30.12	99.10	1.65	17.3	12.98	69.72	8.66	38.83	28.63
N0_C	Center	1.73	34.71	99.17	1.67	13.3	23.88	62.82	8.51	36.95	25.51
(-1) [c]	C-W	1.74	31.92	99.04	1.67	13.8	25.53	60.67	8.24	37.66	25.23
	C-W(2)	1.79	26.64	99.25	1.65	12.0	23.97	64.03	8.38	37.21	26.08
N1_C	Center	1.73	32.85	99.09	1.66	13.0	22.34	64.66	8.44	38.04	26.74
(0/1)	C-W	1.66	38.52	98.95	1.69	13.4	20.58	66.02	8.46	38.23	27.25
	C-W(2)	1.65	37.92	98.80	1.71	14.3	20.18	65.52	8.45	41.12	26.95
N2_C	Center	1.67	36.48	98.54	1.71	17.3	32.44	50.26	8.14	34.60	20.38
(1/4)	C-W	1.70	34.80	98.79	1.69	17.2	31.50	51.30	8.41	34.15	20.51
	C-W(2)	1.69	34.53	98.64	1.70	16.0	29.89	54.11	8.47	34.34	21.44
N3_C	Center	1.68	35.49	98.60	1.70	16.2	26.12	57.68	8.02	37.15	23.87
(1/2)	C-W	1.62	37.74	98.92	1.69	16.8	24.35	58.85	8.25	36.78	23.99
	C-W(2)	1.65	36.99	98.95	1.69	15.8	24.34	59.86	8.30	36.89	24.42

[a] $f_{-2} + f_{LAGB} + f_{HAGB} = 100\%$

[b] wire from the coil of a new cable (service life of 0 years)

As one can see from grain-size distribution histograms (Figures 3a,b,c,d of main text and Figures S4a,b,c,d) consistent with visual inspection expectations, for all aluminum and steel samples, the most widespread grain sizes are $D_{grain} \approx 1.5$ μm (from ≈64% to ≈78% in different samples and areas along the span), the second and third most widespread sizes are $D_{grain} \approx 2.5$ μm (from ≈17% to ≈32%) and $D_{grain} \approx 0.5$ μm (from ≈4% to ≈9%). Grains with sizes $D_{grain} \approx 3.5$ μm and more do not exceed 2%.

Considering the difference between different samples, we note that the maximum fraction of ≈78% of grains with a size of $D_{grain} \approx 1.5$ μm is observed near the edge of the cross-section of the new N0_W-C Al wire in contact with the steel core wire (see Figure 3a of main text). At the same time, in the center of the cross-section and in the zone of contact with the atmosphere (N0_W-A), the fractions of such grains are ≈68% and ≈73%. After 52 years of operation in OPL, the total fraction of grains with sizes $D_{grain} \approx 1.5$ μm changes (see Figure 3b of main text and Figures S4a,b) at the W-C edge, in the center, and at the W-A edge of the cross-section, respectively, to ≈72% (i.e., decreases in comparison to new wire N0_W), ≈74% (i.e., increases), and ≈73% (i.e., not changed) in N1_W (0/1 span), ≈72% (i.e., decreases), ≈70% (i.e., increases), and ≈73% (i.e., not changed) in N2_W (1/4 span), and most strongly decreases down to ≈69%, ≈68%, and ≈64% in N3_W (1/2 span). Simultaneously, at the W-C edge, in the center, and at the W-A edge of the cross-section of Al wires, a corresponding increase in the fraction of certain grains is observed,

namely, with sizes D_{grain} ≈ 2.5 μm and D_{grain} ≈ 0.5 μm to ≈21%, ≈18%, and ≈17% and ≈6%, ≈ 8%, and ≈10%, respectively, in N1_W (0/1 span), ≈21%, ≈21%, and ≈18% and ≈6%, ≈7%, and ≈8% in N2_W (1/4 span), and, most strongly, up to ≈26%, ≈25%, and ≈32% and ≈5%, ≈6%, and ≈4% in N3_W (1/2 span) compared to ≈17%, ≈22%, and ≈21% and ≈5 %, ≈6%, and ≈4% for new N0_W Al wire.

It should be noted that these grain-size-distribution results are qualitatively similar to the results for Al wires from cables of A50 and AC50 types with lifetimes of 0–62 years and 0–20 years, respectively, previously studied in [2, 3, 21], and for Al wires (from cables A50 type) after fatigue tests [22].

In steel wires, the grain size trends are different compared to Al wires. In contrast to the new Al wire, in the new steel wire on average (over the entire cross-section), the fraction of grains with sizes D_{grain} ≈ 1.5 μm is less, whereas that with sizes D_{grain} ≈ 2.5 μm more than in the steel core wire from the cable after 52 years of operation in OPL, while the fraction of grains with sizes D_{grain} ≈ 0.5 μm on average slightly differs up or down (Figures 3c,d of main text and Figures S4c,d) (respectively, at the C-W (and C-W(2)) edge and at the center of the cross-section of the new steel wire N0, the fractions of grains with sizes D_{grain} ≈ 1.5 μm are ≈63% (≈58%) and ≈67%, the fractions of grains with sizes D_{grain} ≈ 2.5 μm are ≈28% (≈23%) and ≈27%; and the fractions of grains with sizes D_{grain} ≈ 0.5 μm are ≈7% (≈7%) and ≈7% versus the fractions of grains ≈72% (≈73%) and ≈65% (D_{grain} ≈ 1.5 μm), ≈22% (≈21%) and ≈28% (D_{grain} ≈ 2.5 μm), and ≈7% (≈7%) and ≈5% (D_{grain} ≈ 0.5 μm) for wire N1_C (0/1 span), ≈64% (≈66%) and ≈68% (D_{grain} ≈ 1.5 μm), ≈26% (≈25%) and ≈23% (D_{grain} ≈ 2.5 μm), and ≈7% (≈7%) and ≈7.5 % (D_{grain} ≈ 0.5 μm) for N2_C (1/4 span), and ≈72% (≈69%) and ≈67% (D_{grain} ≈ 1.5 μm), ≈19% (≈22%) and ≈24% (D_{grain} ≈ 2.5 μm), and ≈8% (≈7.5%) and ≈7% (D_{grain} ≈ 0.5 μm) for N3_C (1/2 span) after 52 years of operation).

As one can see from the grain-size-distribution histograms (Figure 3 of main text and Figure S4), the root mean square (r.m.s.) estimated standard deviations (e.s.d.s) of the average grain sizes $<D_{grain}>$ averaged over all available individual D_{grain} values, for all samples are rather large, ~0.4–0.5 μm. Nevertheless, the average $<D_{grain}>$ grain size seems to systematically change along the length of the OPL span (Figure 7a,b of main text and Table S4).

In the new Al wire N0_W, the average grain sizes at the center of the cross-section ('Center' in Figure 7a of main text) and at its edges at the point of contact with the steel wire (W-C) and with the atmosphere (W-A) are close, although somewhat larger in the center (cf., $<D_{grain}>$ = 1.66 μm, 1.62 μm, and 1.63 μm for Center, W-C, and W-A). After 52 years of service in the OPL, near the clamp on the OPL support (0/1 span), the average grain size decreases the most at the W-A edge of the wire cross-section and the least at the W-C edge (cf., $<D_{grain}>$ = 1.60 μm, 1.64 μm, and 1.58 μm for Center, W-C, and W-A). When moving along the span from the support (0/1 span) to its center (1/2 span), the value of $<D_{grain}>$ in all locations of the cross-section of the Al wire increases rather smoothly to $<D_{grain}>$ = 1.72 μm, 1.73 μm, and 1.79 μm for Center, W-C, and W-A, respectively, mirroring down as it approaches the next pillar (1/1 span). Thus, for the center and W-A and W-C edges of an Al-wire cross-section, the change in $<D_{grain}>$ along the span from one clamp to the next one is close to a Λ-shape (inverted V-shape) with a maximum at the middle of the span.

In the new N0_C steel core wire, the average grain size in the center of the cross-section ('Center' in Figure 7b of main text) and on its edges at the points of contact with the steel wire (C-W and C-W(2)) is noticeably larger than in the Al wire, while at the edge of the cross-section of the steel wire at the point of contact C-W with Al wire and at the center of the cross-section, the average grain sizes are almost the same, whereas at the point of the second contact C-W(2) with Al wire $\langle D_{grain} \rangle$ is the largest (cf., $\langle D_{grain} \rangle$ = 1.73 μm, 1.73 μm, and 1.79 μm for Center, C-W, and C-W(2)). In steel wires, the average grain size $\langle D_{grain} \rangle$ changes along the span from the clamp to the middle in a different way than in Al wires, showing a sawtooth change, antiphase at the center of the cross-section and at its edges. Near the clamp (0/1 span), in the center of the cross-section, the $\langle D_{grain} \rangle$ value is the same as in the new wire, although noticeably decreasing at the edges (cf., $\langle D_{grain} \rangle$ = 1.73 μm, 1.66 μm, and 1.65 μm for Center, C-W, and C-W(2)). Further, at a quarter of the span length, $\langle D_{grain} \rangle$ in the center of the cross-section decreases to 1.67 μm, and on the edges, on the contrary, increases to 1.70 μm (C-W) – 1.69 μm (C-W(2)), changing when moving towards the center of the span (1/2 span) to a slight increase in the center of the cross-section up to 1.68 μm and a noticeable decrease at the edges down to 1.62 μm (C-W) – 1.65 μm (C-W(2)). Finally, the variation of the average grain size in the mirror order occurs when approaching the next OPL support (1/1 span).

Let us dwell now on the change in some other microstructural parameters of aluminum and steel wires of ACSR cable of AC50 brand along the span in more detail.

For ease of analysis, the microstructure parameters of aluminum and steel wires from a 52-year-old OPL cable, which are summarized in Table S4, are also shown graphically in Figure 7 of main text and Figure S7 as a function of position on the span.

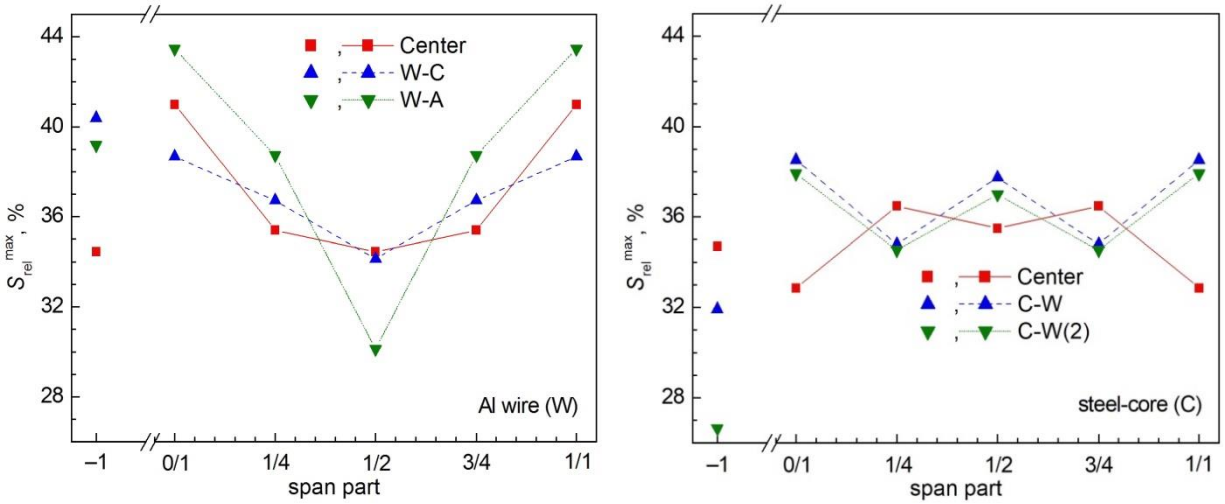

(**a**) (**b**)

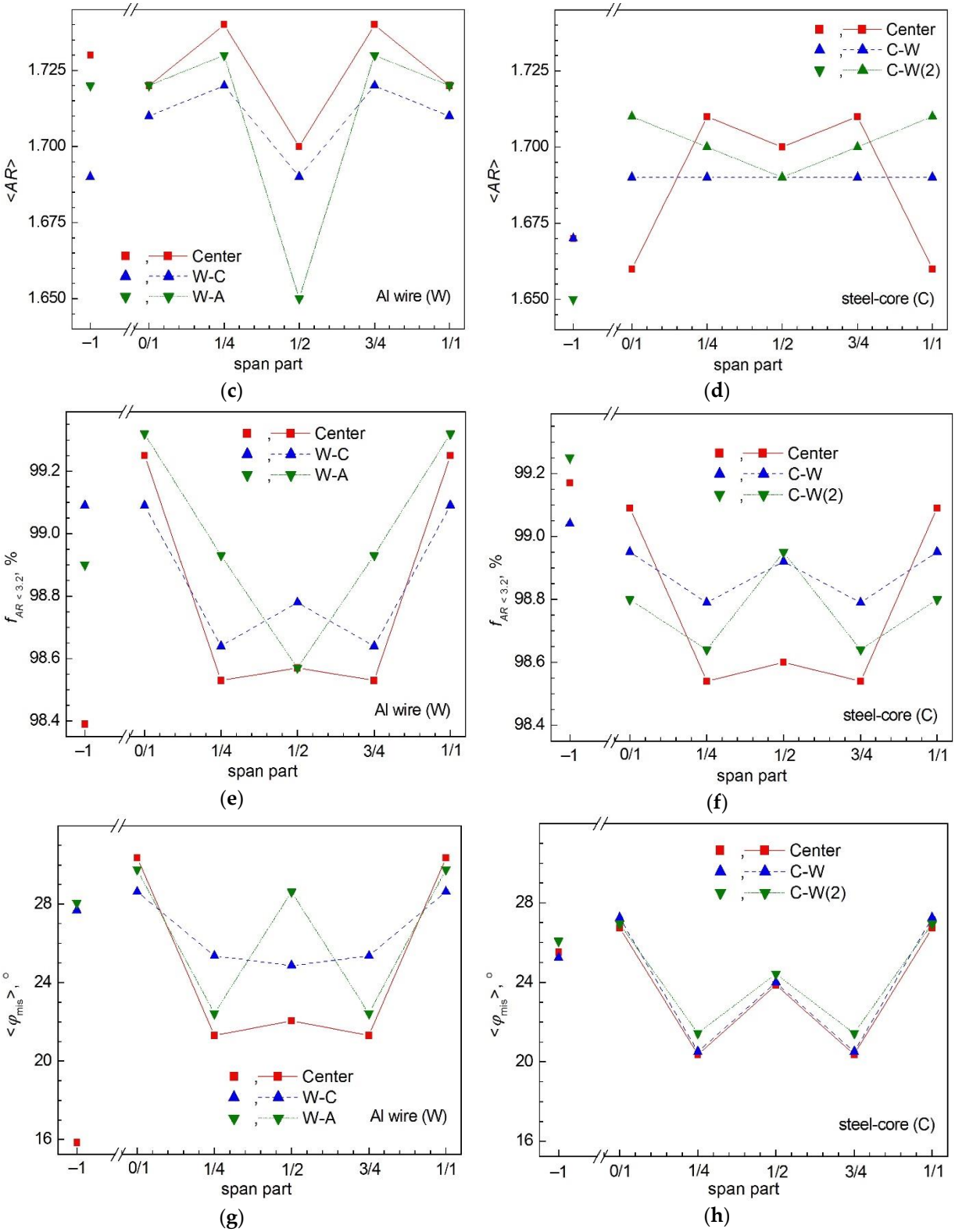

Figure S7. (**a**, **b**) Relative area S_{rel}^{max} occupied by grains with size D_{grain} = 1.95 μm (where maximum of the $S_{rel}(D_{grain})$ dependence is observed), (**c**, **d**) average AR value <*AR*>, (**e**, **f**) grain fraction with AR < 3.2, and (**g**, **h**) mean misorientation angle $<\varphi_{mis}>$ averaged over all observed individual GBs with misorientation angles $\varphi_{mis} \geq 2°$ for (**a**, **c**, **e**, **g**) aluminum wire (W) and (**b**, **d**, **f**, **h**) steel wire core (C) of AC50 cable at different span parts after 52 years of operation in OPL. For comparison, data for new (0 years of service life) are shown at the span position designated as '–1'. Data designated as 'Center' are obtained from the centers of the wire cross-sections. Data designated as W-C and W-A are obtained from areas of aluminum wires near contacts of aluminum wire – steel wire core and

aluminum wire – air, respectively. Data designated as C-W and C-W(2) are calculated from areas of steel wire cores near contacts of steel wire – adjacent aluminum wire and steel wire – adjacent aluminum wire at opposite side of the steel wire.

The relative areas S_{rel} occupied by grains of different size before and after operation in OPLs are nearly bell-shaped (more precisely, like a lognormal distribution) with maxima at $D_{grain} \approx 1.95$ μm for aluminum and steel wires, which are practically independent of the service life and position on the span from where the wires originated (Figures 4a,b of main text and Figures S5a,b). In new wires of both types, the relative areas occupied by grains are approximately the same at the centers of the cross-sections of the wires and amount to $S_{rel} = S_{rel}^{max} \approx 34.5\%$ at the maxima, increasing to ≈40% at the W-C and W-A edges of the Al wire and to ≈27% and 32% at the C-W(2) and C-W edges, respectively, of steel wire (Figure 4a of main text, span '-1' in Figures S7a,b and Table S4).

After 52 years of service, at the centers of Al-wire cross-sections, S_{rel}^{max} increases from 34.44% (new wire) to 40.98% and 35.40% at the clamp (0/1 span) and quarter the span (1/4 span) positions, respectively, remaining virtually unchanged at the center of the span ($S_{rel}^{max} = 34.44\%$ at 1/2 span), see Figure 4b of main text, Figures S5a,b and Figure S7a and Table S4. The in crease in S_{rel}^{max} at the centers of the cross-sections of Al wires from AC50 cable after service is qualitatively consistent with the previously observed trend for long service life [3]. In [3], Al wires from AC50 cable after different service life from 0 to 20 years were studied, cut from the span far from the clamps and from half the span. It has been found that, in contrast to the Al wires from A50 cable without steel core, where there is a decrease in S_{rel}^{max} for all service lives up to 62 years [3, 21] in comparison with the new wires, in Al wires from AC50 cable with a steel wire core after 8 years of service, S_{rel}^{max} decreases from ≈26% to 22% and then increases to 29% after 20 years of operation.

Compared to the new state, at the W-C edges of the cross-sections of Al wires after 52 years of operation, the relative area S_{rel}^{max}, on the contrary, is the smaller the closer to the middle of the span (40.38% in the new wire compared to 38.67%, 36.72%, and 34.13% for span parts = 0/1, 1/4, and 1/2, respectively), whereas at the point of the W-A contact with the air atmosphere, the value of S_{rel}^{max} is higher than in the new state but then drops sharply (39.18% in the new wire compared to 43.47%, 38.73%, and 30.12% for span parts = 0/1, 1/4, and 1/2 respectively, see Figures 4b,c,d of main text, Figure S7a, and Table S4).

For aluminum wire, S_{rel}^{max} over the entire span shows a V-shaped change with a minimum at half the span in contrast to $\langle D_{grain} \rangle$ characterized by a reverse, Λ-shaped, change with a maximum at half the span (cf. Figure 7a of main text and Figure S7a).

For steel wire, the S_{rel}^{max} dependence on span part qualitatively replicates the $\langle D_{grain} \rangle$ dependence on span part for all contacts (Center, C-W, and C-W(2)), although reversed (cf. Figure 7b of main text and Figure S7b). For a steel core wire compared to Al wire, the scatter of minimum and maximum values is 1.5–2 times smaller. At the center of the cross-section along the span, S_{rel}^{max} shows an M shape with a minimum value of 32.85% near the clamps (0/1 span) rising to 36.48% at a quarter the span (1/4 span) and dropping to 35.49% at half the span (1/2 span). At the C-W and C-W(2) contacts of steel wire with aluminum, the change in S_{rel}^{max} appears to be inverted, W-shaped, with close values

(S_{rel}^{max} = 37.92%–38.52%, 34.53%–34.80%, and 36.99%–37.74% for span parts = 0 /1, 1/4, and 1/2).

Thus, the change in the relative area S_{rel}^{max} occupied by grains of size D_{grain} = 1.95 μm, which cover the largest area, occurs along the span between OPL supports in antiphase with the change in the average grain size $<D_{grain}>$ for both types of wires, aluminum and steel (cf. Figures 7a,b of main text and Figures S7a,b).

As in aluminum wires from A50 cables of the AAAC type that have served from 0 to 62 years in OPL [3, 21] or after fatigue testing [22], as well as from AC50 cables of the ACSR type [3], AR histograms of grains in the center and on the cross-sectional edges of the new wire and the wire after 52 years of operation are very similar and change insignificantly along the span between the OPL supports (Figures 5a,b,c,d of main text and Figures S6a,b,c,d). Moreover, this qualitative statement is true for both aluminum wire and steel one cut from AC50 cable.

A quantitative study, which is more sensitive to detecting changes, has shown that the average $<AR>$ value of the AR value of aluminum wires changes systematically nonetheless and is close to the antiphase change with a variation in the average grain size $<D_{grain}>$, i.e., the $<AR>$ value shows the decrease at the span part where $<D_{grain}>$ is increasing (cf. Figures 7a,b of main text and Figures S7a,b). Thus, $<AR>$ reaches its minimum at half the span (1/2 span), most noticeable at the W-A contact of the Al wire with the air atmosphere ($<AR>$ = 1.73, 1.72, and 1.65 for, respectively, Center, W-C, and W-A of 1/2-span sample in comparison to the corresponding values $<AR>$ = 1.72, 1.74 (0/1 span), 1.71, 1.72 (1/4 span), and 1.72, 1.73 (1/2 span), see Table S4 and Figure S7c). At the same time, for the steel wire core (see Figure S7d of main text and Table S4), at least for the C-W contact, a correlation is not found (the $<AR>$ value is constant for all span parts and equal to 1.69). For the second contact, C-W(2), there is a gradual drop in $<AR>$ from 1.71 to 1.69 when moving from the cable clamps (0/1 span) to half the span (1/2 span). At the midpoint of the cross-section (Center) of the steel wire, the behavior of the $<AR>$ dependence on the span part is similar to the behavior of $<AR>$ for Al wire, when $<AR>$ first increases towards a quarter the span and then decreases on the way to half the span, showing an M-shape ($<AR>$ = 1.66, 1.71, and 1.70 for span parts = 0/1, 1/4, and 1/2, respectively), which is opposite in phase to the W-shaped $<D_{grain}>$ change at the center of the wire (cf., Figure 7b of main text and Figure S7d). It should be noted that the average values of $<AR>$ in most cases are very close along the span (especially for span parts '0/1' and '1/4'). Therefore, further studies are needed to confirm the statistical significance of the obtained dependences of $<AR>$ on the span part. So far, we can only talk about trends that correlate with changes in other parameters of the microstructure.

The similarity or practical invariance of AR histograms indicates that, regardless of either the service life or the position on the span or in the cross section, the grain shape in aluminum and steel wires practically does not change. Note that the observed AR values range from 1 to 5 for all samples. However, as in the aforementioned studies of Al wires from A50 from AC50 cables of different service life or processing [2, 3, 21, 22], in the cross-sections of both types of wires studied (aluminum and steel wires, new and 52 years old in OPL cable), the overwhelming fraction of AR values for all samples is less than AR = 3.2 ($f_{AR<3.2}$ = 98.39%–99.32% in aluminum wires and 98.54%–99.17% in steel wires, see Table S4 of

Supporting Materials). Just as in the case of <*AR*>, one can note that, for aluminum and steel wires, there is a correlation between $f_{AR<3.2}$ and the average grain size $\langle D_{grain} \rangle$ along the span. Variation $f_{AR<3.2}$ shows a W-shape (or V-shape in case of W-A contact of Al wire, which can be considered as a degenerate W-shape). Additionally, for all contacts in the case of aluminum wire (Center, W-C, and W-A) and for contacts C-W and C-W(2) of steel wire, the dependences of $f_{AR<3.2}$ and $\langle D_{grain} \rangle$ on the span part are antiphase or close to antiphase, whereas the correlations $f_{AR<3.2}$ and $\langle D_{grain} \rangle$ are in phase for the centers of the cross-sections of the steel wire. (cf. Figures 7a,b of main text and Figures S7e,f). However, since the difference in $f_{AR<3.2}$ values along the span is small for wires of both types as in the case of <*AR*>, the presence of a correlation requires additional statistical confirmation.

S2.4. Results of XRD

Tabulated crystallographic data (unit cell parameters a, b, c, α, β, and γ) of the observed crystalline phases according to PDF-2 database are summarized in Table S5. In the Table S5, estimated standard deviations (e.s.d.s) are given if they are given in the reference cited. Penetration depths T_{pen} estimated according to formula (S2) are summarized in Table S6. Half of the maximum Bragg angle $2\theta_B^{max}$, where the reflections attributed to the phase are observed in XRD patterns (Figures 8 and 9 of the main text) was used to obtain the T_{pen} estimates.

Table S5. Crystallographic data of the crystalline phases observed for aluminum and steel wires (at room temperature) according to PDF-2 database.
[a]

Crystalline phase	Space group	a, Å α, °	b, Å β, °	c, Å γ, °	PDF-2 card Ref.
Al	The line absorption	$Fm\bar{3}m$ (225)	4.04932(2)	a	a	01-073-9843
		90	α	α	[14]
δ-Al_2O_3		$P4_12_12$ (92)	7.9631(7)	a	23.3975(23)	00-056-1186
		90	α	α	[11]
δ^*-Al_2O_3		$P222$ (16)	7.934	7.956(1)	11.711(6)	00-066-1215
		90	α	α	[12]
Zn		$P6_3/mmc$ (194)	2.6677(9)	a	4.934(5)	01-080-4436
		90	α	120	[15]
ZnO		$Fm\bar{3}m$ (225)	4.270(9)	a	a	01-073-8589
		90	α	α	[16]
ZnO_2		$Pa\bar{3}$ (205)	4.871(6)	a	a	01-076-1364
		90	α	α	[17]
Fe		$Im\bar{3}m$ (229)	2.8664	a	a	00-006-0696
		90	α	α	[18]
α-FeO		$Fm\bar{3}m$ (225)	4.285(2) [a]	a	a	01-080-3819
		90	α	α	[19]
γ-Fe_2O_3		$P4_32_12$ (96)	8.346	a	25.034	01-089-5894
		90	α	α	[20]

coefficient μ_l calculated for a modification of δ-Al_2O_3 (tetragonal space group $P\bar{4}m2$ (115)) [13] was used for estimation of T_{pen}.
[a] at temperature of 318 K

Table S6. Estimated penetration depths T_{pen} for Cu-K_α radiation and maximum Bragg angle $2\theta_B^{max}$, where the reflections attributed to the crystalline phase are observed for different samples.

Sample	Phase	T_{pen}, μm	$2\theta_{B\ max}$, °	PDF-2 card	Ref.
N0_W-A	Al	35.47	137.44	01-073-9843	[14]
N0_W-C	Al	35.47	137.44	01-073-9843	[14]
N1_W-A	Al	35.47	137.43	01-073-9843	[14]
N1_W-A	δ-Al_2O_3	10.84 [a]	31.59	00-056-1186	[11]
N1_W-A	δ*-Al_2O_3	10.80 [a]	31.59	00-066-1215	[12]
N1_W-C	Al	35.47	137.43	01-073-9843	[14]
N1_W-C	δ-Al_2O_3	23.81 [a]	73.43	00-056-1186	[11]
N1_W-C	δ*-Al_2O_3	23.81 [a]	73.43	00-066-1215	[12]
N1_W-C	γ-Fe_2O_3	2.85	73.43	01-089-5894	[20]
N2_W-A	Al	35.48	137.45	01-073-9843	[14]
N2_W-A	δ-Al_2O_3	24.33 [a]	75.34	00-056-1186	[11]
N2_W-A	δ*-Al_2O_3	24.25 [a]	75.34	00-066-1215	[12]
N2_W-C	Al	35.48	137.50	01-073-9843	[14]
N2_W-C	δ-Al_2O_3	22.33 [a]	68.22	00-056-1186	[11]
N2_W-C	δ*-Al_2O_3	22.25 [a]	68.22	00-066-1215	[12]
N2_W-C	γ-Fe_2O_3	2.67	68.22	01-089-5894	[20]
N3_W-A	Al	35.47	137.39	01-073-9843	[14]
N3_W-A	δ-Al_2O_3	10.87 [a]	31.67	00-056-1186	[11]
N3_W-A	δ*-Al_2O_3	10.83 [a]	31.67	00-066-1215	[12]
N3_W-C	Al	35.47	137.38	01-073-9843	[14]
N3_W-C	δ-Al_2O_3	9.22 [a]	26.77	00-056-1186	[11]
N3_W-C	δ*-Al_2O_3	9.19 [a]	26.77	00-066-1215	[12]
N3_W-C	γ-Fe_2O_3	2.02	50.21	01-089-5894	[20]
N0_C-W	Zn	10.85	138.28	01-080-4436	[15]
N0_C-W	ZnO	13.27	138.28	01-073-8589	[16]
N0_C-W	ZnO_2	16.55	110.26	01-076-1364	[17]
N0_C-W	Fe	1.75	116.33	00-006-0696	[18]
N0_C-W	α-FeO	1.74	61.42	01-080-3819	[19]
N0_C-W	γ-Fe_2O_3	4.45	137.28	01-089-5894	[20]
N1_C-W	Zn	9.86	116.38	01-080-4436	[15]
N1_C-W	ZnO	8.56	74.18	01-073-8589	[16]
N1_C-W	ZnO_2	11.02	66.23	01-076-1364	[17]
N1_C-W	Fe	1.92	137.23	00-006-0696	[18]
N1_C-W	α-FeO	2.04	73.60	01-080-3819	[19]
N1_C-W	γ-Fe_2O_3	4.44	137.29	01-089-5894	[20]
N1_C-W	δ-Al_2O_3	26.21 [a]	82.32	00-056-1186	[11]
N1_C-W	δ*-Al_2O_3	26.12 [a]	82.32	00-066-1215	[12]
N2_C-W	Zn	9.85	116.16	01-080-4436	[15]
N2_C-W	ZnO	10.29	92.88	01-073-8589	[16]
N2_C-W	ZnO_2	14.20	89.50	01-076-1364	[17]
N2_C-W	Fe	1.92	137.08	00-006-0696	[18]
N2_C-W	α-FeO	2.47	92.88	01-080-3819	[19]
N2_C-W	γ-Fe_2O_3	4.43	137.08	01-089-5894	[20]
N3_C-W	Zn	9.86	116.36	01-080-4436	[15]
N3_C-W	ZnO	10.31	93.11	01-073-8589	[16]
N3_C-W	ZnO_2	14.37	90.80	01-076-1364	[17]
N3_C-W	Fe	1.92	137.22	00-006-0696	[18]

N3[a]_C-W	α-FeO	2.13	77.53	01-080-3819	[19]
N3_C-W	γ-Fe_2O_3	4.43	137.22	01-089-5894	[20]
N3_C-W	δ-Al_2O_3	26.22 [a]	82.35	00-056-1186	[11]
N3_C-W	δ^*-Al_2O_3	26.13 [a]	82.35	00-066-1215	[12]

linear absorption coefficie[a] linear absorption coefficient μ_l calculated for a modification of δ-Al_2O_3 (tetragonal space group $P\bar{4}m2$ (115)) [13] was used for estimation of T_{pen}

The numerical values of the structural and microstructural parameters obtained from the analysis of XRD patterns are presented in Table S7.

Table S7. Results [a] of XRD analysis of Al wires from the AC50 ACSR-type cable at different span parts between OPL supports (temperature of XRD measurements is T_{meas} = 314±1 K).

				WHP	**SSP**
Sample	$I_{max}^{022}/I_{max}^{111}$, % [b,c] $I_{max}^{002}/I_{max}^{022}$, % [b,c]	a, Å ρ_x, g/cm³ [b,c]	D_0, nm (for ε_s = 0)	D, nm/ε_s, % R_{cod}, %	D, nm/ε_s, % R_{cod}, %
N0_W-A	54.7(8) 88(1)	4.0501(1) 2.6975(1)	85(12)	85(12)/0 52.04	83(4)/0.011(18) 98.28
N0_W-C	34.8(3) 154(1)	4.0501(1) 2.6976(1)	93(12)	95(9)/0.009(14) 1.59	93(12)/0 99.50
N1_W-A	82.7(7) 58.4(6)	4.0517(8) 2.6945(10)	84(15)	84(15)/0 19.30	84(9)/0.014(29) 92.27
N1_W-C	355(6) 44.2(6)	4.0517(8) 2.6945(10)	81(9)	81(9)/0 15.60	81(9)/0 97.73
N2_W-A	80.5(7) 95.2(8)	4.0498(1) 2.6981(1)	88(12)	88(12)/0 3.73	114(8)/0.032(6) 97.81
N2_W-C	210(2) 46.4(4)	4.0487(2) 2.7005(3)	98(8)	98(8)/0 2.06	110(5)/0.020(6) 98.43
N3_W-A	115(1) 74.0(9)	4.0509(2) 2.6960(3)	83(15)	83(15)/0 17.00	83(5)/0.015(2) 97.31
N3_W-C	134(1) 54.6(8)	4.0496(7) 2.6986(9)	85(13)	101(12)/0.027(7) 36.74	116(6)/0.034(4) 97.97

[a] $I_{max}^{022}/I_{max}^{111}$ and $I_{max}^{002}/I_{max}^{022}$ are observed ratios of the maximum intensities of reflections with Miller indices hkl = 022 and 111 and with hkl = 002 and 022, respectively; a is the parameter of the cubic unit cell of the Al wire material, determined using XRD data; ρ_x is the XRD mass density estimated from the a value; t_{eff} is the effective service life estimated using the ρ_x value; D_0 is the mean size of crystallites in the model without microstrains (ε_s = 0), obtained by averaging the individual crystallite sizes D_0^{hkl} estimated for reflections with Miller indices hkl using the Scherrer equation; D and ε_s are, respectively, mean size of crystallites and absolute mean value of microstrain in them according to the results of WHP and SSP methods; R_{cod} is the coefficient of determination obtained for the WHP and SSP graphs.

[b] According to PDF-2 card 01-071-4008 [23] for powder Al, $I_{max}^{022}/I_{max}^{111}$ = 23.9, $I_{max}^{002}/I_{max}^{022}$ = 190.8 at T_{meas} = 197.2 K and a = 4.050694 Å at T_{meas} = 312.3 K, which corresponds to ρ_x = 2.69642 g/cm³.

[c] According to PDF-2 card 01-073-9843 [14] for powder Al at T_{meas} = 298 K, $I_{max}^{022}/I_{max}^{111}$ = 24.0, $I_{max}^{002}/I_{max}^{022}$ = 191.7 and a = 4.04932(2) Å, which corresponds to ρ_x = 2.6992(4) g/cm³.

Figure S8 demonstrates the effect of preferential orientation in the investigated aluminum wires. The changes in the ratio of the maximum intensities of Al reflections with Miller indices hkl = 002 and 022 in the

new aluminum wire and in the wire after 52 years of operation in sections along the span between the OPL supports are shown in comparison with the tabular value for Al powder without preferential orientation from the PDF-2 database (see also Table S7).

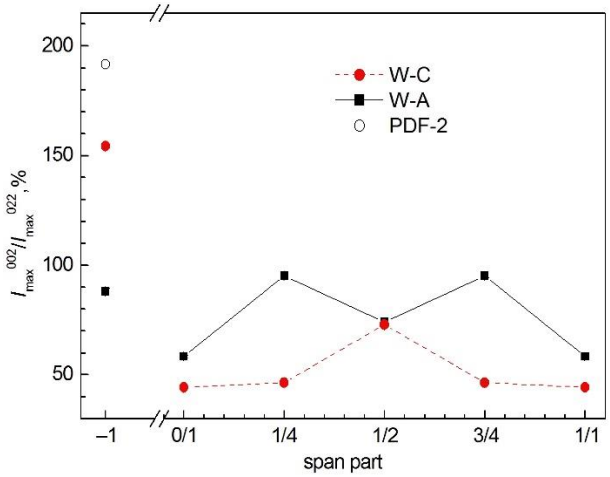

Figure S8. Change in the $I_{max}^{002}/I_{max}^{022}$ ratio along the span for the aluminum wire (for W-A and W-C sides of the wire) from the AC50 cable after 52 years operation in OPL. Lines connecting the experimental points are guides to the eye only. The $I_{max}^{002}/I_{max}^{022}$ ratio values observed for unused new Al wire are shown at the span position '–1'. The data marked as PDF-2 correspond to PDF-2 card 01-073-9843 of Al powder without influence of effects of preferential orientation.

In contrast to the ratio $I_{max}^{022}/I_{max}^{111}$, the value of which in the new aluminum wire N0 is greater than in the tabulated Al powder (Table S7 and Figure 10 of the main text of this paper), the value of $I_{max}^{002}/I_{max}^{022}$ in this wire is less ($I_{max}^{002}/I_{max}^{022} \approx 154\%$ and 88 % for wire sides W-C and W-A, respectively, compared to $I_{max}^{002}/I_{max}^{022} \approx 192\%$ for tabulated Al powder. After 52 years of operation, the ratio $I_{max}^{002}/I_{max}^{022}$ has decreased even more (to $I_{max}^{002}/I_{max}^{022} \approx 44\%–73\%$ and 58 %–95% for W-C and W-A, respectively), reflecting the development of the preferential orientation along the [011] direction (recall that the $I_{max}^{022}/I_{max}^{111}$ ratio, on the contrary, has increased, see Section 3.4.1 of the main text of this paper). The change in $I_{max}^{002}/I_{max}^{022}$ along the span shows a shape close to V-shaped for side W-C and M-shaped for W-A in comparison with Λ-shaped and V-shaped changes in $I_{max}^{022}/I_{max}^{111}$, respectively (cf. Figure 10 of the main text and Figure S8).

Figure S9 and Table S7 show the calculated cubic unit cell parameter a of the aluminum material of a new wire and that of a wire after 52 years of service for sides W-A and W-C (more precisely, as discussed in Section 2.2 in the case of the XRD method, the cubic parameter a of the Al material of the wire near-surface layer with a thickness equal to the penetration depth of the Cu-K_α radiation used, $T_{pen} \approx 36$ μm). The horizontal line in this Figure S9 shows the value $a_{exp} = 4.0557(2)$ Å which is expected after 52 years of operation in AC50 OPL cable while maintaining the corrosion rate $v_a = 1.07(3)\cdot10^{-4}$ Å/year found in [3] for aluminum wires from AC50 cables after operation from 0 to 20 years ($a_{exp} = a_0 + v_a t$, where a_0 (in Å) is unit cell parameter of the Al material of new unused aluminum wire and t is the service life of an AC50 cable (in years)). Another horizontal line in Figure S9 shows the table value $a_{table} = 4.050694$ Å for the Al powder, which is borrowed from the PDF-2 database (card 01-071-4008) [23] and obtained at a measurement temperature $T = 312.3$ K, close to the XRD measurement temperature $T = 314 \pm 1$ K in the present study.

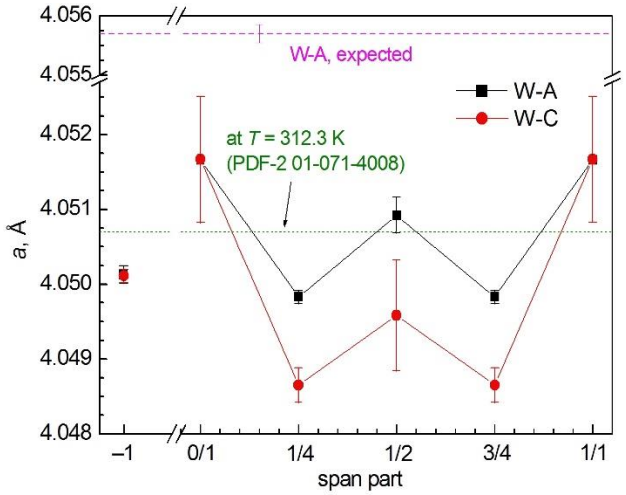

Figure S9. Change in the cubic unit cell parameter a along the span for the aluminum wire (for W-A and W-C sides of the wire) from the AC50 cable after 52 years operation in OPL. The values obtained for unused new Al wire are shown at the span position '–1'. Lines connecting the experimental points are guides to the eye only. Horizontal lines of different style correspond to parameter a_{table} of the table Al powder obtained from the XRD measurements at 312.3 K (PDF-2 card 01-071-4008 and Ref. [23]) and parameter a_{exp} expected from the linear law obtained in [3] for Al material of W-A side of aluminum wires from AC50 cable after 0–20 years of service life in OPL.

As one can see from Figure S9 and Table S7, the cubic unit cell parameter of the aluminum wire material in the new state, a_0, is almost the same for the W-C and W-A sides of the wire. After 52 years of service in OPL cable, parameter a increases at both W-C and W-A contacts at the span edges (span parts '0/1' and '1/1'), remaining greater than a_0 for W-A also at midspan (1/2 span). This increase in the parameter a is in qualitative agreement with the lattice expansion of the Al material previously found in [3] for the W-A sides of aluminum wires from AS50 cables with lifetimes from 0 to 20 years. At the same time, at 1/4 and 3/4 of the span, the value of parameter a for the W-A side drops to a value smaller than the value of a_0 in the new sample. As a result, the dependence function of the parameter a of the Al material of the wire W-A side along the span becomes W-shaped (Figure S9). For the W-C side of the Al wire, the parameter a also varies along the span, following a W-shaped function, but both with a larger difference between the maximum values (at the edges, span parts '0/1' and '1/1') and minimum ones (span parts '1/4' and '3/4') and with a larger dip below a_0 at midspan (1/2 span).

Figure S10 and Table S7 show the crystallite size D_0 calculated in the model without microstrains ($\varepsilon_s = 0$) and obtained by root-mean-square averaging of individual crystallite values for each reflection, estimated according to the Scherrer law (with a coefficient $K_{Scherrer} = 0.94$) from the values of full width at half maximum intensity (FWHM) of the observed reflections, $FWHM_{corr}$, corrected for instrumental broadening using the [24–26] procedure according to the pseudo-Voigt (pV) type of reflections observed in XRD patterns. The XRD reflections of the Al material of wires were assigned to the pV type based on the found $FWHM/B_{int}$ ratio ranging from 0.636 to 0.939 [27] (Figure S11), where $FWHM$ is the observed FWHM (uncorrected for instrumental broadening) and B_{int} is the integrated reflex width. The functions of dependences of D_0 on the position on the span show an M-shaped form, however, e.s.d.s of D_0 are too large (Figure S10), which may be due to not only the experimental

e.s.d.s of the determined $FWHM_{corr}$ values but also because of the contribution of microstrains in reflection broadening (Figure S11).

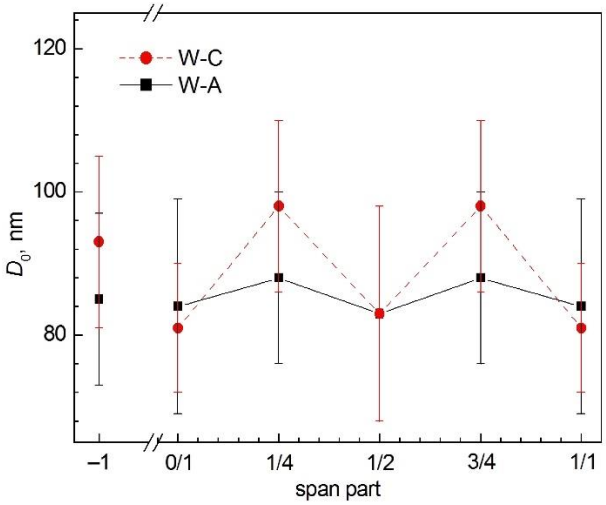

Figure S10. Change in the Al-crystallite size D_0 calculated in the model of the microstrain absence ($\varepsilon_s = 0$) along the span for the aluminum wire (for W-A and W-C sides of the wire) from the AC50 cable after 52 years of operation in OPL. The values obtained for unused new Al wire are shown at the span position '–1'. Lines connecting the experimental points are guides to the eye only.

Figure S11 shows the WHP and SSP plots for Al material of new (unused) wires from AC50 cable and wires of AC50 cable after 52 years of service. In WHP and SSP analyses, coefficients $K_{Scherrer} = 0.94$ and $K_{strain} = 4$ were used. The found approximating straight lines $Y = A + B \cdot X$ for the WHP and SSP methods are indicated in the graphs of Figure S11, where X and Y are expressions composed of the parameters of the observed reflections with Miller indices hkl ($FWHM_{corr}$, cosines, and sines (WHP) or cosines (SSP) of half the Bragg angle $\theta_B = 2\theta_B/2$ and, in the case of SSP, the interplanar distance d_{hkl}) and the wavelength λ of the Cu-$K_{\alpha 1}$ radiation (upon correcting for the Cu-$K_{\alpha 2}$ contribution). Expressions for X and Y are given, respectively, on the abscissa and ordinate axes of the WHP and SSP plots. The values of the average sizes D of crystallites and the absolute average microstrains ε_s in them, calculated from the values of the coefficients A and B of the approximating straight lines (see [24–26]), are also shown in Figures S11a,b,c,d,e,f,g,h,i,j,k,l,m,n,o,p and in Table S7.

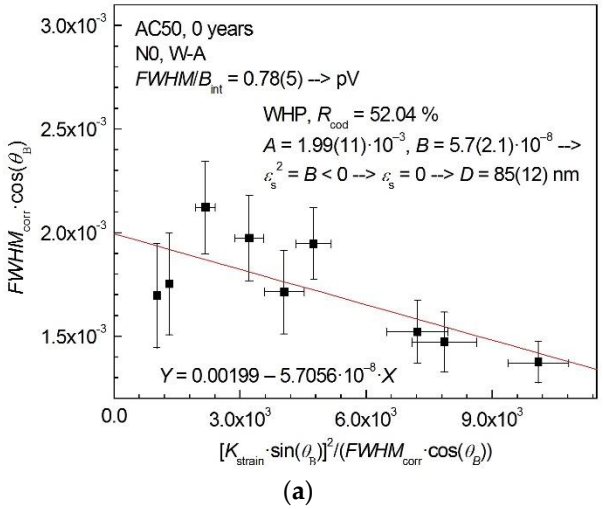

(**a**)

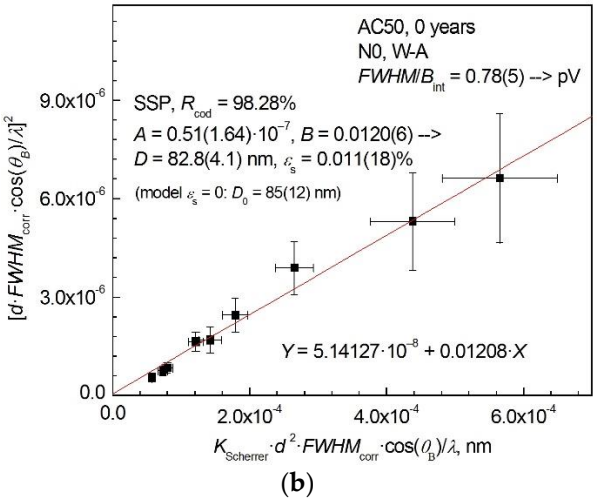

(**b**)

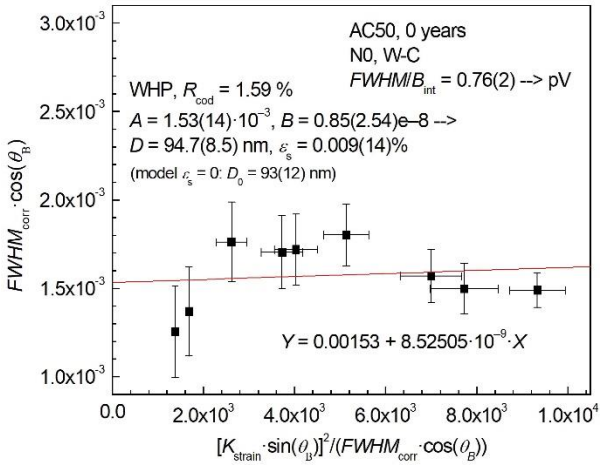
AC50, 0 years
N0, W-C
FWHM/B_int = 0.76(2) --> pV
WHP, R_cod = 1.59 %
A = 1.53(14)·10^-3, B = 0.85(2.54)e–8 -->
D = 94.7(8.5) nm, ε_s = 0.009(14)%
(model ε_s = 0: D_0 = 93(12) nm)
Y = 0.00153 + 8.52505·10^-9·X
FWHM_corr·cos(θ_B)
[K_strain·sin(θ_B)]^2/(FWHM_corr·cos(θ_B))

(**c**)

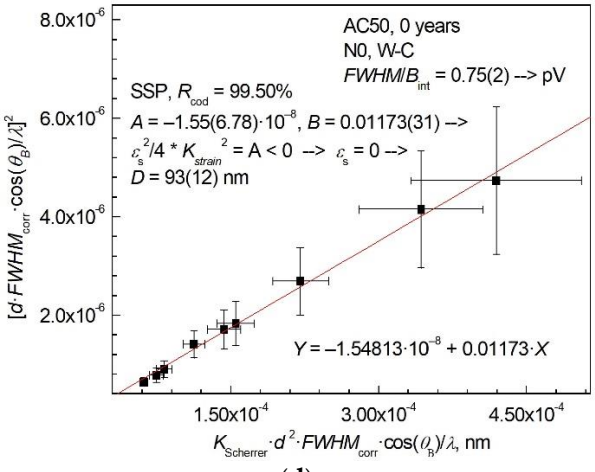
AC50, 0 years
N0, W-C
FWHM/B_int = 0.75(2) --> pV
SSP, R_cod = 99.50%
A = –1.55(6.78)·10^-8, B = 0.01173(31) -->
ε_s^2/4 * K_strain^2 = A < 0 --> ε_s = 0 -->
D = 93(12) nm
Y = –1.54813·10^-8 + 0.01173·X
[d·FWHM_corr·cos(θ_B)/λ]^2
K_Scherrer·d^2·FWHM_corr·cos(θ_B)/λ, nm

(**d**)

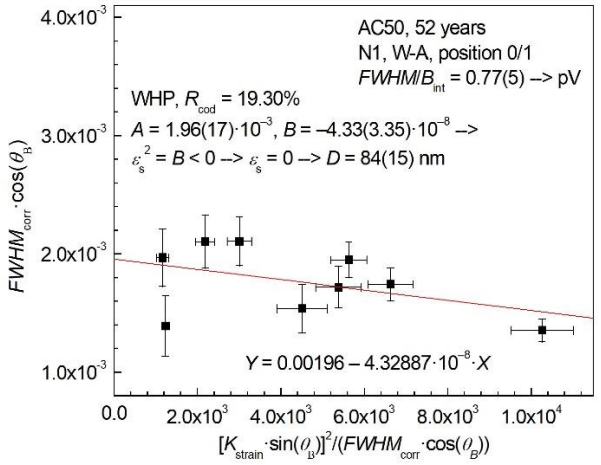
AC50, 52 years
N1, W-A, position 0/1
FWHM/B_int = 0.77(5) --> pV
WHP, R_cod = 19.30%
A = 1.96(17)·10^-3, B = –4.33(3.35)·10^-8 -->
ε_s^2 = B < 0 --> ε_s = 0 --> D = 84(15) nm
Y = 0.00196 – 4.32887·10^-8·X
FWHM_corr·cos(θ_B)
[K_strain·sin(θ_B)]^2/(FWHM_corr·cos(θ_B))

(**e**)

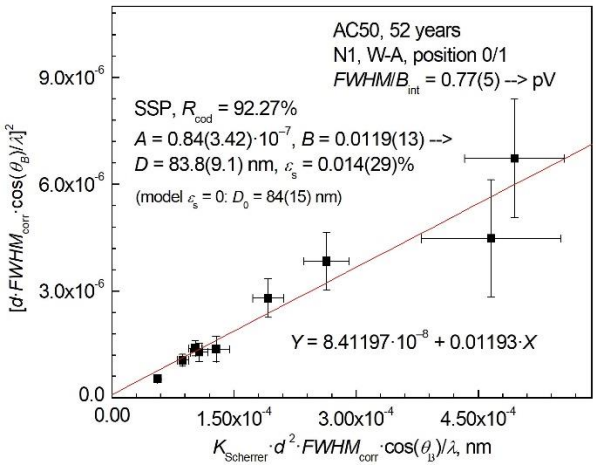
AC50, 52 years
N1, W-A, position 0/1
FWHM/B_int = 0.77(5) --> pV
SSP, R_cod = 92.27%
A = 0.84(3.42)·10^-7, B = 0.0119(13) -->
D = 83.8(9.1) nm, ε_s = 0.014(29)%
(model ε_s = 0: D_0 = 84(15) nm)
Y = 8.41197·10^-8 + 0.01193·X
[d·FWHM_corr·cos(θ_B)/λ]^2
K_Scherrer·d^2·FWHM_corr·cos(θ_B)/λ, nm

(**f**)

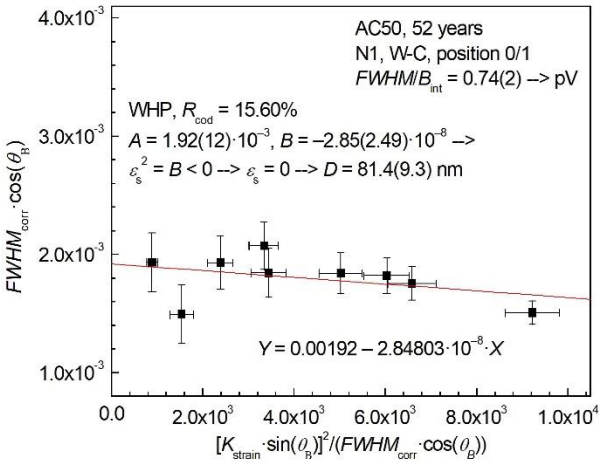
AC50, 52 years
N1, W-C, position 0/1
FWHM/B_int = 0.74(2) --> pV
WHP, R_cod = 15.60%
A = 1.92(12)·10^-3, B = –2.85(2.49)·10^-8 -->
ε_s^2 = B < 0 --> ε_s = 0 --> D = 81.4(9.3) nm
Y = 0.00192 – 2.84803·10^-8·X
FWHM_corr·cos(θ_B)
[K_strain·sin(θ_B)]^2/(FWHM_corr·cos(θ_B))

(**g**)

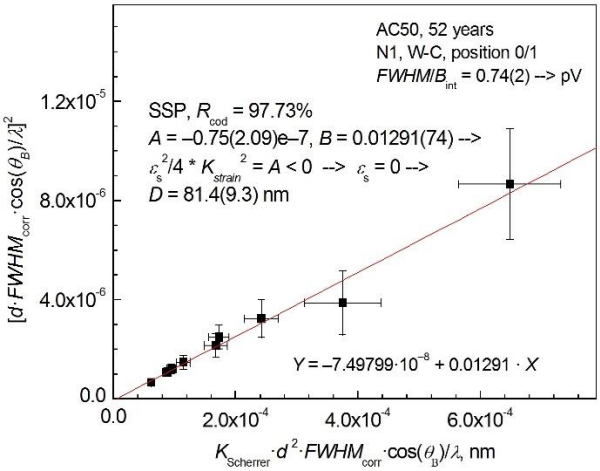
AC50, 52 years
N1, W-C, position 0/1
FWHM/B_int = 0.74(2) --> pV
SSP, R_cod = 97.73%
A = –0.75(2.09)e–7, B = 0.01291(74) -->
ε_s^2/4 * K_strain^2 = A < 0 --> ε_s = 0 -->
D = 81.4(9.3) nm
Y = –7.49799·10^-8 + 0.01291 · X
[d·FWHM_corr·cos(θ_B)/λ]^2
K_Scherrer·d^2·FWHM_corr·cos(θ_B)/λ, nm

(**h**)

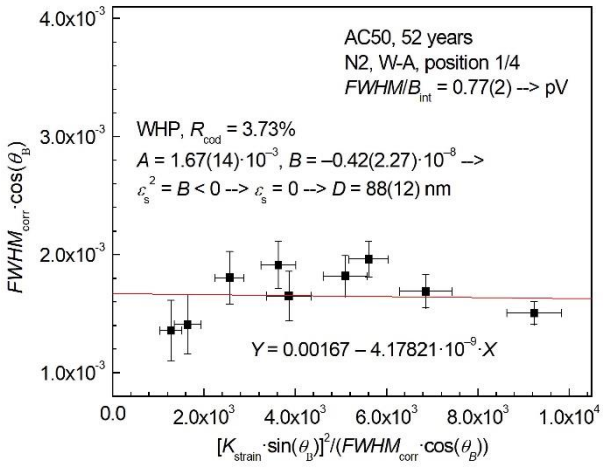
AC50, 52 years
N2, W-A, position 1/4
FWHM/B_int = 0.77(2) --> pV
WHP, R_cod = 3.73%
A = 1.67(14)·10^-3, B = –0.42(2.27)·10^-8 -->
ε_s^2 = B < 0 --> ε_s = 0 --> D = 88(12) nm
Y = 0.00167 – 4.17821·10^-9·X
FWHM_corr·cos(θ_B)
[K_strain·sin(θ_B)]^2/(FWHM_corr·cos(θ_B))

(i)

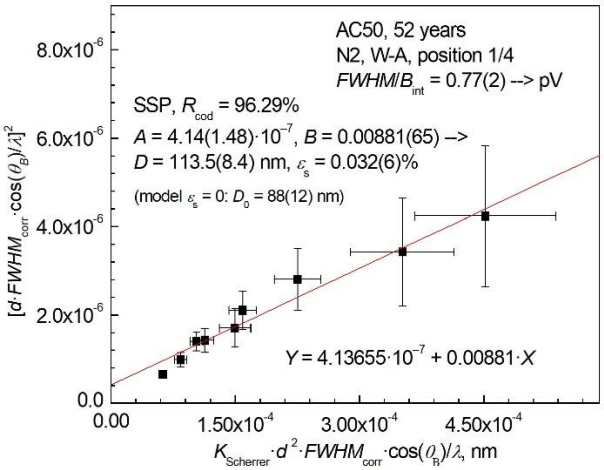
AC50, 52 years
N2, W-A, position 1/4
FWHM/B_int = 0.77(2) --> pV
SSP, R_cod = 96.29%
A = 4.14(1.48)·10^-7, B = 0.00881(65) -->
D = 113.5(8.4) nm, ε_s = 0.032(6)%
(model ε_s = 0: D_0 = 88(12) nm)
Y = 4.13655·10^-7 + 0.00881·X
[d·FWHM_corr·cos(θ_B)/λ]^2
K_Scherrer·d^2·FWHM_corr·cos(θ_B)/λ, nm

(j)

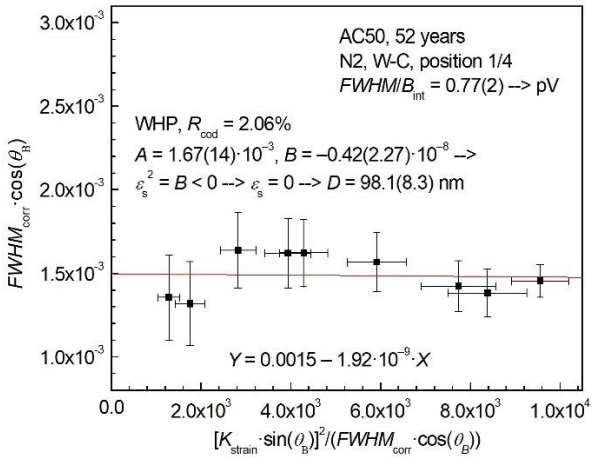
AC50, 52 years
N2, W-C, position 1/4
FWHM/B_int = 0.77(2) --> pV
WHP, R_cod = 2.06%
A = 1.67(14)·10^-3, B = –0.42(2.27)·10^-8 -->
ε_s^2 = B < 0 --> ε_s = 0 --> D = 98.1(8.3) nm
Y = 0.0015 – 1.92·10^-9·X
FWHM_corr·cos(θ_B)
[K_strain·sin(θ_B)]^2/(FWHM_corr·cos(θ_B))

(k)

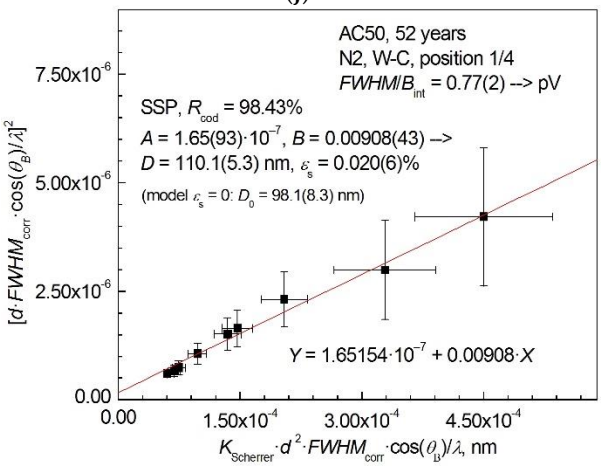
AC50, 52 years
N2, W-C, position 1/4
FWHM/B_int = 0.77(2) --> pV
SSP, R_cod = 98.43%
A = 1.65(93)·10^-7, B = 0.00908(43) -->
D = 110.1(5.3) nm, ε_s = 0.020(6)%
(model ε_s = 0: D_0 = 98.1(8.3) nm)
Y = 1.65154·10^-7 + 0.00908·X
[d·FWHM_corr·cos(θ_B)/λ]^2
K_Scherrer·d^2·FWHM_corr·cos(θ_B)/λ, nm

(l)

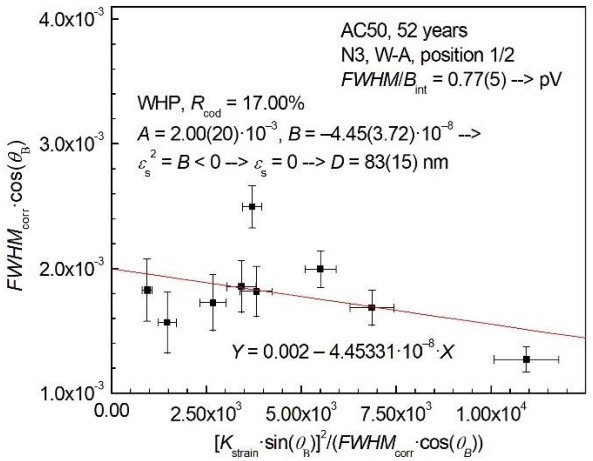
AC50, 52 years
N3, W-A, position 1/2
FWHM/B_int = 0.77(5) --> pV
WHP, R_cod = 17.00%
A = 2.00(20)·10^-3, B = –4.45(3.72)·10^-8 -->
ε_s^2 = B < 0 --> ε_s = 0 --> D = 83(15) nm
Y = 0.002 – 4.45331·10^-8·X
FWHM_corr·cos(θ_B)
[K_strain·sin(θ_B)]^2/(FWHM_corr·cos(θ_B))

(m)

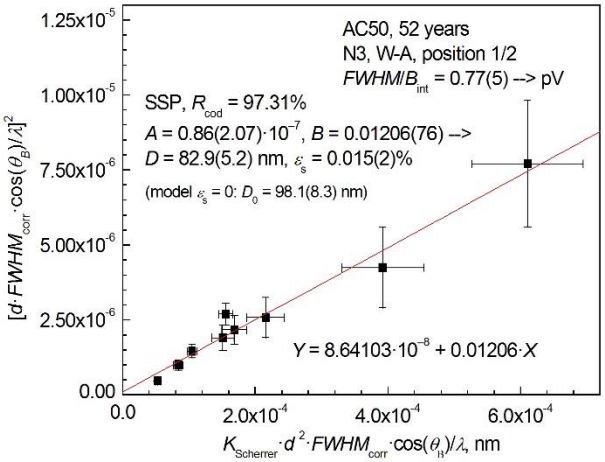
AC50, 52 years
N3, W-A, position 1/2
FWHM/B_int = 0.77(5) --> pV
SSP, R_cod = 97.31%
A = 0.86(2.07)·10^-7, B = 0.01206(76) -->
D = 82.9(5.2) nm, ε_s = 0.015(2)%
(model ε_s = 0: D_0 = 98.1(8.3) nm)
Y = 8.64103·10^-8 + 0.01206·X
[d·FWHM_corr·cos(θ_B)/λ]^2
K_Scherrer·d^2·FWHM_corr·cos(θ_B)/λ, nm

(n)

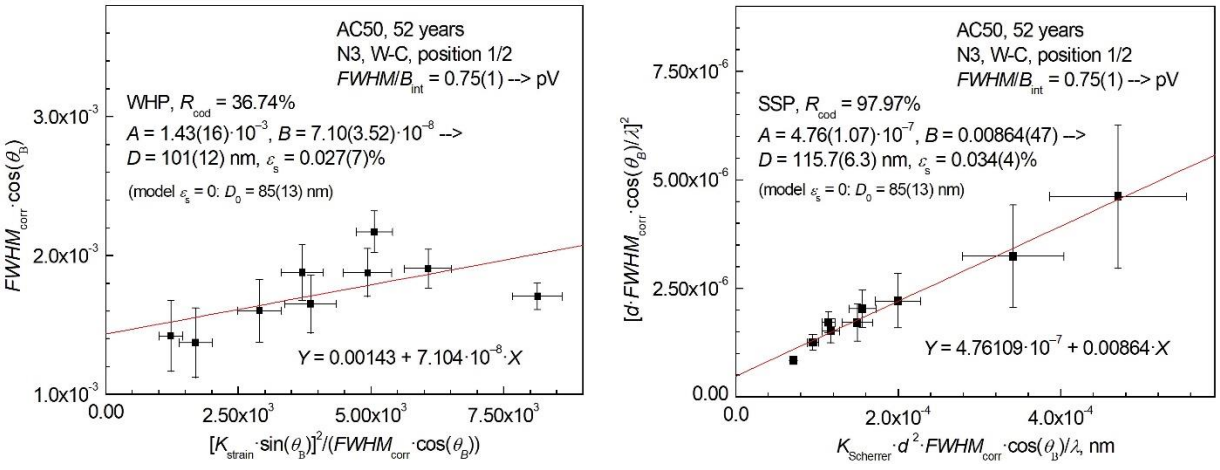

(**o**) (**p**)

Figure S11. (**a, c, e, g, i, k, m, o**) WHP plots and (**b, d, f, h, j, l, n, p**) SSP ones constructed for the aluminum wire sides W-A (**a, b, e, f, i, j, m, n**) and W-C (**c, d, g, h, k, l, o, p**) contacted, respectively, with air and steel core wire. New aluminum wire N0 (**a, b, c, d**) and aluminum wire after 52 years of operation in OPL: (**e, f, g, h**) N1 (0/1 span), (**i, j, k, l**) N2 (1/4 span), and (**m, n, o, p**) N3 (1/2 span).

S2.5. Results of acoustics measurements

Numerical results of acoustic measurements are presented in Table S8.

Table S8. Young's modulus *E*, amplitude-independent decrement of elastic vibrations δ_i, and microplastic flow stress σ_s of aluminum and steel wire samples prepared from AC50 OPL cables depending on the span position (according to results of acoustic measurements at room temperature).

Sample	Material	Part of span	*E*, GPa	$\delta_i \cdot 10^5$	σ_s, MPa [a]
N0_W	Al	−1[b]	71.40	21.6	9.3
N1_W	Al	0/1	71.43	37.3	8.7
N2_W	Al	1/4	71.19	46.5	7.2
N3_W	Al	1/2	71.71	54.2	8.1
N0_C	Steel	1[b]	211.67	218	14.2
N2_C	Steel	1/4	206.53	76.2	7.5
N3_C	Steel	1/2	207.05	34.3	14.5

[a] the σ_s values correspond to inelastic deformation $\varepsilon_d = 1 \cdot 10^{-8}$ for aluminum and $3 \cdot 10^{-9}$ for steel.

S.3. Discussion

S3.1 Comparison of elemental and phase content according to EDX and XRD in current research and in literature data

As noted in the main text of this paper, data on the elemental (EDX) and phase (XRD) composition of W-A surfaces (i.e. external surfaces exposed to the atmosphere) of aluminum wires from A50 AAAC and AC50 ACSR cables of different service life from 8 to 62 years [2, 3, 21] are in good agreement with those obtained in this work for aluminum wire from AC50 ACSR cable after 52 years of operation. Let us consider how the data obtained agree with the known EDX and XRD data from other studies [28–31].

According to EDX analysis (Table 3 of the main text), on W-A surfaces (exposed to air) of samples N1 (0/1 span), N2 (1/4 span), and N3 (1/2 span) after 52 years of service in the OPL cable, in addition to Al and O, which prevailed in weight content, the presence of S (0.99 wt.% to

1.24 wt.%), Cl (0.00 wt.% to 1.06 wt.%), K (0.47 wt.% to 0.56 wt.%), and Fe (1.33 wt.% to 3.01 wt.%) was detected. In [28–31], when studying the surfaces of aluminum wires of the outer layer (i.e., W-A surfaces too) of various modifications of ACSR cables of different service life from 29 to 61 years by means of the EDX method, in addition to dominant Al and O, various dopants were found, namely, Cl, K, Fe, and Cu in [28], P, C, and S in [29] (quantities not specified), C, Mg, P, S, K, and Fe in [30] and Si (5.20 wt.% to 6.98 wt. %), P (0.50 wt.% to 1.22 wt.%), S (7.50 wt.% to 8.50 wt.%), Fe (2.50 wt.% to 7.63 wt.%), and Zn (0.40 wt. % to 0.85 wt.%) in [31].

S.3.2. Estimation of density of dislocations in aluminum wires from AC50 cable after 52 years of operation in OPL

According to [32], the dislocation density in metals

$$L_{dis} = \frac{2\sqrt{3}\varepsilon_s}{D \cdot b}, \quad \text{(S5)}$$

where D is the average size of regions of coherent X-ray scattering (i.e., crystallites), ε_s is the absolute value of the average microstrain in them, and b is the Burgers vector of the dislocation.

As an example, let us consider the aluminum wires from AC50 cable before and after 52 years of operation in OPL, which are analyzed in this paper and for which the values of D and ε_s are determined for both the W-A and W-C sides of these wires in different parts of the span (Table S7 and Figure 12 of main text). To obtain trends in L_{dis}, one can estimate the normalized values

$$L_{dis}^{norm} = \frac{L_{dis}}{L_{dis0}}, \quad \text{(S6)}$$

which makes it possible to get rid of the need to know the Burgers vector (assuming it to be a constant value). As L_{dis0} one can take any non-zero minimum value, i.e., consider a wire where ε_s is nonzero but minimum. For example, it is convenient to take $D \approx 83$ nm and $\varepsilon_s \approx 0.01\%$ for the W-A side of a new aluminum wire as normalizing values (N0_W-A, Table S7 and Figure 12 of main text). Then the normalized dislocation density L_{dis}^{norm} shows how many times the dislocation density L_{dis} is greater or less on each part of the span in comparison with the dislocation density L_{dis0} on the W-A side of the aluminum wire from the new cable. Estimates based on the data of Table S7 lead to M-shaped and Λ-shaped distribution functions of the normalized dislocation density L_{dis}^{norm} (and, accordingly, those of the dislocation density L_{dis}) for W-A and W-C sides of the aluminum wires, respectively (Figure S12). The distribution functions of the dislocation density obtained in this way are fully similar to the distribution functions of microstrain ε_s over span parts, as one can see from the comparison of Figure 12 of the main text and Figure S12.

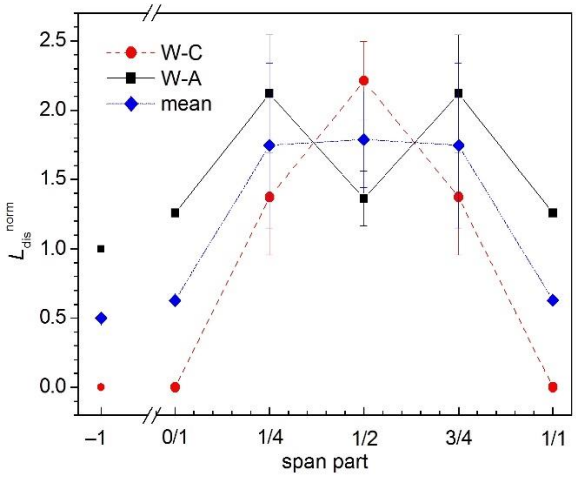

Figure S12. Change in the normalized dislocation density L_{dis}^{norm} along the span for the aluminum wire (for W-A and W-C sides of the wire and averaged over W-A and W-C sides) from the AC50 cable after 52 years of operation in OPL. The values obtained for unused new Al wire are shown at the span position '–1'. Lines connecting the experimental points are guides to the eye only.

Thus, exploitation of wires in an AC50-type OPL cable results in a maximum dislocation density at a quarter of the span and a noticeable but moderate value in the middle for the W-A side of the aluminum wire. For the W-C side, the situation is reversed, i.e., there is a maximum of L_{dis} at the middle of the span and a smaller, though not minimum, value at a quarter of the span. Taking into account the stabilization of D and ε_s at depths greater than ~30 μm from the surface [2, 3], one can consider the values of the dislocation density L_{dis}^{mean} averaged over the L_{dis} values for the W-A and W-C sides. This average density L_{dis}^{mean} is characterized by approximately the same maximum value at a quarter and in the middle of a span (Figure S12).

References

1. Nikanorov, S. P.; Kardashev, B. K. *Elasticity and Dislocation Inelasticity of Crystals*; Nauka: Moscow, Russia, 1985; 256 p. (in Russian)
2. Narykova, M. V.; Levin, A. A.; Prasolov, N. D.; Lihachev, A. I.; Kardashev, B. K.; Kadomtsev, A. G.; Panfilov, A. G.; Sokolov, R. V.; Brunkov, P. N.; Sultanov, M. M.; Kuryanov, V. N.; Tyshkevich, V. N. The structure of the near-surface layer of the AAAC overhead power line wires after operation and its effect on their elastic, microplastic, and electroresistance properties, *Crystals* **2022**, *12*, 166. doi: 10.3390/cryst12020166
3. Levin, A.A.; Narykova, M.V.; Lihachev, A.I.; Kardashev, B.K.; Kadomtsev, A.G.; Prasolov, N.D.; Panfilov, A.G.; Sokolov, R.V.; Brunkov, P.N.; Sultanov, M.M.; Strizhichenko, A.V.; Boldyrev, I.A. Comparison of structural, microstructural, elastic, and microplastic properties of the AAAC (A50) and ACSR (AC50/8) cables after various operation periods in power transmission line. *Crystals* **2022**, *12*, 1267. doi: 10.3390/cryst12091267
4. Lukiyanov, F.A.; Rau, E.I.; Sennov, R. A. Depth Range of Primary Electrons, Electron Beam Broadening, and Spatial Resolution in Electron-Beam Studies. *Bull. Russ. Acad. Sci.: Phys.* **2009**, *73*, 463–472. doi: 10.3102/s1062873809040029
5. Kanaya, K.; Okayama, S. Penetration and energy-loss theory of electrons in solid targets. *J. Phys. D: Appl. Phys.* **1972**, *5*, 43–58. doi: 10.1088/0022-3727/5/1/308
6. International Centre for Diffraction Data (ICDD). *Powder Diffraction File-2 Release 2014*, ICDD: Newton Square, PA, USA, 2014
7. Nakhimova, L.I. (Ed.) *GOST 839-2019. Non-Insulated Conductors for Overhead Power Lines. Specifications*. Strojizdat: Moscow, Russia, 2019; 39 p. (in Russian)
8. Fundamental Physical Constants. NIST, Gaithersburg, MD, USA. Available online: https://physics.nist.gov/cgi-bin/cuu/Value?na|search_for=Avogadro (accessed on 02 February 2023)

9. Kraus, W.; Nolze, G. POWDER CELL - a program for the representation and manipulation of crystal structures and calculation of the resulting X-ray powder patterns. *J. Appl. Crystallogr.* **1996**, *29*, 301–303. doi: 10.1107/S0021889895014920
10. Merkys, A.; Vaitkus, A.; Grybauskas, A.; Konovalovas, A.; Quirós, M.; Gražulis, S. Validation of the Crystallography Open Database using the Crystallographic Information Framework. *J. Appl. Crystallpogr.* **2021**, *54*, 661–672. doi: 10.1107/S1600576720016532
11. Tsybulya, S.; Kryukova, G. New X-ray powder diffraction data on δ-Al_2O_3. *Powder Diffr.* **2003**, *18*, 309–311. doi: 10.1154/1.1604128
12. Fargeot, D.; Mercurio, D.; Dauger, A. Structural characterization of alumina metastable phases in plasma sprayed deposits. *Mater. Chem. Phys.* **1990**, *24*, 299. doi: 10.1016/0254-0584(90)90093-P
13. Repelin, Y.; Husson, E. Etudes structurales d'alumines de transition. I – Alumines gamma et delat. *Mater. Res. Bull.* **1990**, *25*, 611–625 (in French). doi: 10.1016/0025-5408(90)90027-Y
14. Miller Jr, P. H.; DuMond, J. W. M. Tests for the Validity of the X-Ray Crystal Method for Determining N and e with Aluminum,
15. Martinez, O.; Hortelano, V.; Jimenez, J.; Plaza, J.L.; de Dios, S.; Olvera, J.; Dieguez, E.; Fath, R.; Lozano, J.G.; Ben, T.; Gonzalez, D.; Mass, J. Growth of Zn O nanowires through thermal oxidation of metallic zinc films on Cd Te substrates. *J. Alloys Compds.* **2011**, *509*, 5400–5407. doi: 10.1016/j.jallcom.2011.02.063
16. Karzel, H.; Potzel, U.; Potzel, W.; Moser, J.; Schaefer, C.; Steiner, M.; Peter, M.; Kratzer, A.; Kalvius, G.M. X-ray diffractometer for high pressure and low temperatures. *Mater. Sci. Forum.* **1991**, *79*, 419–426. doi: 10.4028/www.scientific.net/MSF.79-82.419
17. Vannenberg, N.G. Formation and structure of zinc peroxide. *Ark. Kemi* **1959**, *14*, 119.
18. Swanson, H.E.; Tatge, E. Standard X-Ray Diffraction Powder Patterns. *Natl. Bur. Stand. (U. S.)* **1955**, Circ. 539 IV, 3.
19. Crisan, O.; Crisan, A. Phase transformation and exchange bias effects in mechanically alloyed Fe/magnetite powders. *J. Alloys Compds.* **2011**, *509*, 6522–6527. doi: 10.1016/j.jallcom.2011.03.147
20. Shin, H.-S. A study on the structure of maghemite (gamma-(Fe_2O_3)). I. Rietveld analysis pf powder XRD patterns. J Korean Ceram. Soc. **1998**, 35, 1113–1119.
21. Levin, A.A.; Narykova, M.V.; Lihachev, A.I.; Kardashev, B.K.; Kadomtsev, A.G.; Brunkov, P.N.; Panfilov, A.G.; Prasolov, N.D.; Sultanov, M.M.; Kuryanov, V.N.; Tyshkevich, V.N. Modification of the structural, microstructural, and elastoplastic properties of aluminum wires after operation, *Metals* **2021**, *11* 1955. doi: 10.3390/met11121955
22. Levin, A.A.; Narykova, M.V.; Lihachev, A.I.; Kardashev, B.K.; Kadomtsev, A.G.; Panfilov, A.G.; Prasolov, N.D.; Sokolov, R.V.; Brunkov, P.N.; Sultanov, M.M.; Strizhichenko, A.V.; Boldyrev. I.A. Structural, Microstructural, Elastic, and Microplastic Properties of Aluminum Wires (from AAAC (A50) Cables) after Fatigue Tests. *Metals* **2023**, *13*, 298. doi: 10.3390/met13020298
23. Otte, H. M.; Montague, W. G.; Welch, D. O. X-ray diffractometer determination of the thermal expansion coefficient of aluminum near room temperature. *J. Appl. Phys.* **1963**, *34*, 3149–3150. doi: 10.1063/1.1729148
24. Terlan, B.; Levin, A.A.; Börrnert, F.; Simon, F.; Oschatz, M.; Schmidt, M.; Cardoso-Gil, R.; Lorenz, T.; Baburin, I.A.; Joswig, J.-O.; et al. Effect of Surface Properties on the Microstructure, Thermal, and Colloidal Stability of VB_2 Nanoparticles. *Chem. Mater.* **2015**, *27*, 5106–5115. doi: 10.1021/acs.chemmater.5b01856
25. Terlan, B.; Levin, A. A.; Börrnert, F.; Zeisner, J.; Kataev, V.; Schmidt, M.; Eychmüller, A. A Size-Dependent Analysis of the Structural, Surface, Colloidal, and Thermal Properties of $Ti_{1-x}B_2$ (x = 0.03–0.08) Nanoparticles. *Eur. J. Inorg. Chem.* **2016**, *2016*, 3460–3468. doi: 10.1002/ejic.201600315
26. Levin, A.A. Program *SizeCr* for Calculation of the Microstructure Parameters from X-ray Diffraction Data. Preprint. 2022. doi: 10.13140/RG.2.2.15922.89280
27. Langford, J. I.; Cernik, R. J.; Louer, D. The Breadth and Shape of Instrumental Line Profiles in High-Resolution Powder Diffraction. *J. Appl. Phys.* **1991**, *24*, 913–919. doi: 10.1107/S0021889891004375
28. Azevedo, C. R. F.; Cescon, T. Failure analysis of aluminum cable steel reinforced (ACSR) conductor of the transmission line crossing the Paranar River. *Eng. Fail. Anal.* **2002**, *9*, 645–664. doi: 10.1016/S1250-6307(02)00021-3d
29. Lequien, F.; Auzoux, Q.; Moine, G.; Rousseau, M.; Pasquier-Tilliette, S.; Holande, A.; Ammi, S.; Heurtault, S.; Prieur, P. Characterization of an aluminum conductor steel reinforced (ACSR) after 60 years of operation, *Eng. Fail. Anal.* **2021**, *120*, 105039. doi: 10.1016/j.engfailanal.2020.105039
30. Achiriloaiei, D.; Medeleanu, M. Studies on the Effects of Environmental Pollution on ACSR Conductors, *Rev. de Chim.* **2019**, *70*, 3984–3986. doi: 10.37358/rc.19.11.7687
31. Kreislova, K.; Jaglova, M.; Turek L., Koukalova, A. Evaluation of corrosion of long-term exposed aluminium conductor. *Koroze Ochr. Mater.* **2013**, *57*, 25–34. doi: 10.2478/v10227-011-0025-4

32. Williamson, G.K., Smallman, R.E. III. Dislocation densities in some annealed and cold-worked metals from measurements on the X-ray Debye-Scherrer spectrum. *Philos. Mag.* **1956**, *1*, 34–46. doi: 10.1080/14786435608238074